2023-05-01

Characterization of novel self-healing polymer blends for additive manufacturing

Truman James Word
University of Texas at El Paso

CHARACTERIZATION OF NOVEL SELF-HEALING

POLYMER BLENDS FOR ADDITIVE

MANUFACTURING

TRUMAN JAMES WORD

Doctoral Program in Materials Science and Engineering

APPROVED:

David A. Roberson, Ph.D., Chair

Robert C. Roberts, Ph.D.

Darren Cone, M.S.

Stephen L. Crites, Jr., Ph.D.
Dean of the Graduate School

CHARACTERIZATION OF NOVEL SELF-HEALING

POLYMER BLENDS FOR ADDITIVE

MANUFACTURING

by

TRUMAN JAMES WORD

DISSERTATION

Presented to the Faculty of the Graduate School of

The University of Texas at El Paso

in Partial Fulfillment

of the Requirements

for the Degree of

DOCTOR OF PHILOSOPHY

Materials Science and Engineering

THE UNIVERSITY OF TEXAS AT EL PASO

May 2023

Acknowledgements

"One bite at a time"

Abstract

This dissertation begins with an overview of novel polymer systems which have been developed by the Polymer Extrusion Lab at the University of Texas at El Paso. Many composite polymer systems have been created using many different polymers as well as ceramics and metals primarily in the form of powders added to the bulk polymer. The bulk of this work entails a study that was conducted to develop and characterize the mechanical, shape memory and self-healing properties of three polymer blends: polylactic acid (PLA) combined with maleated styrene-ethylene-butylene-styrene (SEBS-g-MA), acrylonitrile butadiene styrene (ABS) combined with maleated styrene-ethylene-butylene-styrene (SEBS-g-MA), and polylactic acid (PLA) combined with thermoplastic polyurethane (TPU). These blends were melt compounded at a 50% by weight ratio in a twin-screw extruder into filament for use in desktop FFF style 3D printers. Additively manufactured test samples were made using the extruded filament and injection molded samples were made after pelletizing the filament. The three polymer blends were evaluated in both 3D printed and injection molded forms to determine their mechanical and shape memory properties. To evaluate the shape memory properties, samples were tested for tensile strength in their as-fabricated forms and compared to their tensile strength after being subjected to 25%, 50%, and 100% elongation of their gauge length. This was done for samples in both additively manufactured and injection molded forms both with and without being allowed to dwell under load at the prescribed amount of elongation. The averages of the tensile strength for each polymer blend in both manufacturing forms were plotted against the amount of deformation from which they were recovered. A line of best fit was generated for each and the slope of the equation was divided by the y-intercept to generate a value we are calling the "self-healing parameter" that indicates the percent of baseline tensile strength which is lost after being recovered from 100% elongation.

Table of Contents

List of Tables

List of Figures

Chapter 1: Novel Polymer Material Systems to Expand the Abilities of FDM™-type Additive Manufacturing

Chapter 1 of this dissertation was published in MRS Communications' April 2021 special issue on Polymers for Additive Manufacturing Perspective [1] *and is reproduced with permission from Springer Nature. Written permission has also been granted and the license for use of the article "Novel polymer materials systems to expand the capabilities of FDM™-type additive manufacturing" is shown in the appendix.*

The work presented here describes the efforts conducted in the past decade by the Polymer Extrusion Lab at The University of Texas at El Paso in the area of novel materials development for fused deposition modeling (FDM™)-type additive manufacturing platforms. Here, we discuss efforts in the development of application-specific material systems as well as the development of material systems whose physical properties can be enhanced by FDM™-Type processing. Additional efforts in the area of hybrid composite materials, sustainable materials and shape memory polymers are discussed. Aspects related to materials characterization are also highlighted.

Introduction

Widespread adoption of additive manufacturing (AM) technologies over the past two decades has significantly changed the way wide varieties of objects are made. However, the transition from a budding manufacturing technology to terminology used in the common vernacular (usually referred to as 3D printing) has not corresponded to widespread development and proliferation of new materials. Take, for example, the additive manufacturing platform of fused deposition modeling, (FDM™) also referred to as fused filament fabrication (FFF) when non-trademarked versions of the technology are used. The ubiquity of FFF machines, which found proliferation aided by open-source movements such as RepRap [2–3] and the expiration of patents

on FDM™ technology in 2009 [4], means versions of this AM platform can be found in many K-12 institutions, universities, industrial settings, and the garage laboratories of hobbyists and do-it-yourselfers. However, the most common feedstock material has been and continues to be acrylonitrile butadiene styrene (ABS) [5]. There is a materials palette of commercially available thermoplastic filaments, such as various polylactic acid (PLA) matrix composites filled with wood, coffee as well as copper, bronze and other metals (allowing for a lustrous metallic finish after a polishing post-processing step) offered by companies such as Proto-pasta (ProtoPlant, Vancouver, WA, USA). In this same vein, The Virtual Foundry (Stoughton, WI, USA) offers extremely highly-loaded PLA filaments that enable the printing of green bodies which can then be sintered to form metallic objects. This in turn enables metal additive manufacturing to be performed on the relatively inexpensive FFF platform as compared to powder-bed fusion platforms such as electron beam melting (EBM) or selective laser sintering (SLS). There are also several commercially available variations of carbon fiber filled thermoplastics such as Nylon and ABS. Stratasys (Rehovot, Israel) also offers an electrostatic discharge (ESD) ABS filament, and other manufacturers have also made ESD materials from polycarbonate (PC) and glycol-modified polyethylene terephthalate (PETG). Thermoplastic urethanes (TPU) that are physically flexible as well as high strength, high glass transition temperature (T_g) filaments such as polyether ether ketone (PEEK) are also commercially available.

Though there has been a fair amount of materials developed for FFF processes by industry, these materials are mainly composites where the matrix material is a common thermoplastic such as ABS or Nylon. Academia has been the primary creator of new material systems for FDM™-type additive manufacturing platforms. Several instances of the development of application-specific material systems exist in literature where the strategy of creating polymer matrix

composite systems is the main tactic used with filler materials driving the resulting physical properties. For example, Masood and Song [6–7] developed nylon/iron composites for injection molding where the addition of iron particles enhanced the heat dissipation ability as compared to unfilled nylon. Khatri et al. demonstrated the development of a composite composed of ABS loaded with barium titanate ($BaTiO_3$) with the intent of creating materials for dielectric applications where the permittivity of the composite is driven by the filler content [8]. A material system intended for energy storage applications was demonstrated by Kim et al. [9] where a polyvinylidene difluoride (PVDF) matrix was loaded with a combination of multi-walled carbon nanotubes (MWCNT) and $BaTiO_3$. A work by Tambralimath et al. showed that the thermal stability of polycarbonate-ABS (PC-ABS) FDM™ feedstock material increased with the addition of graphene [10].

Beyond somewhat exotic applications such as dielectric and energy storage, there are also several examples of creating FFF-compatible composite material systems for the classical example of maintaining mechanical strength. In these instances, ABS has been combined with filler materials such as carbon fibers [11] and MWCNTs [12]. The development of high strength composites has been mirrored in industry, as there are commercial ABS, PLA, and Nylon filaments loaded with carbon fibers available through Amazon.com.

 The work presented here explores research conducted over the past decade by the Polymer Extrusion Lab (PEL) at The University of Texas at El Paso (UTEP) in the area of novel FFF-compatible polymer blends and polymer matrix composites. We will discuss examples of application-specific composite systems as well as efforts to create environmentally sustainable composites. We will also discuss the creation of novel polymeric blends and cover the research avenues opened by this materials development strategy. Finally, we will discuss characterization

techniques used by our group to understand the interaction between the AM processing and the resultant physical properties.

Experimental Overview

The material systems discussed in this work were created through a melt compounding process. The primary equipment set used was a Collin ZK 25T twin screw extruder/compounder (Collin Lab and Pilot Solutions, Norcross, GA, USA). The unit was equipped with co-rotating intermeshing screws and a melt pump as well as a belt puller/winding system. We have found the melt pump to be extremely critical in the maintaining of a constant filament diameter, which was targeted at 1.75mm or 2.85mm depending on the model of FFF unit used for a given study. On some occasions, particularly when small quantities of material were available (on the order of 100g), a desktop grade Filabot EX2 single screw extruder was used (Filabot, Barre, VT, USA).

Mechanical testing was carried out in the form of tensile testing following the geometries outlined in the ASTM D638 Standard [13] where, in most cases, the Type IV or Type V parameters were used. In some instances, Izod impact testing was also carried out following the ASTM D256 Standard [14] and using a Tinius Olsen IT 504 Impact Tester (Tinius Olsen, Horsham, PA, USA). To fabricate the test specimens, we have used several FFF platforms including a Rostock MAX (SeeMe CNC, Ligonierm, IN, USA), a MakerBot Replicator (MakerBot Industries, Brooklyn, NY, USA) and a Lulzbot Taz series printer (Aleph Objects, Loveland, CO, USA).

Electron microscopy has been the primary method to acquire visual data. We have relied on low vacuum systems, namely a Hitachi TM-1000 tabletop scanning electron microscope (SEM) and a Hitachi SU 3500 variable pressure SEM (Hitachi America, Santa Clara, CA, USA). Both systems are equipped with backscatter electron (BSE) detectors, however the SU 3500 is also equipped with an ultra variable detector (UVD), that allows for imaging analogous to secondary

electron-generated images. Another key aspect of the SU 3500 SEM, is the ability to operate in a low vacuum mode that allows for SEM characterization of specimens without the need to coat the specimens with a conductor. Additionally, our SU 3500 instrument is also equipped with a scanning transmission electron microscopy (STEM) detector (Deben UK, Ltd, London, England), which allowed for phase characterization of the polymer blends discussed in this study. Thin sections for STEM microanalysis were created via cryo-ultramicrotomy where we used a RMC PT-X ultramicrotome (Boeckeler Instruments, Tucson AZ, USA) equipped with a CR-X cryosectioning unit and diamond knife.

THE BASIC STRATEGY FOR CREATING NEW MATERIAL SYSTEMS

The main strategies employed by our group have been to create polymer matrix composites where the matrix material is a commonly used material in FFF processes, such as ABS, Polycarbonate (PC), or PLA, as well as the compounding of novel thermoplastic polymer blends. Both strategies depend on the resulting material system exhibiting physical properties that are a combination of the constituents. For example, the equation describing the yield strength of a composite is given by:

$$\sigma_c = V_{fm}\sigma_m + V_{fr}\sigma_r, \tag{1}$$

where σ_c is the yield strength of the composite, V_{fr}, is the volume fraction of the reinforcing material, V_{fm} is the volume fraction of the matrix, σ_m is the ultimate tensile strength of the matrix and σ_r is the ultimate tensile strength of the reinforcing material [15]. Though we present the example of yield strength, the end goal of making thermoplastic matrix composites for FFF platforms is not always an increase in mechanical strength. In the example of a polymer blend, the expected glass transition temperature can be calculated from the equation:

$$\frac{1}{T_{g\,blend}} = \frac{x_1}{T_{g1}} + \frac{x_2}{T_{g2}}, \tag{2}$$

known as Fox's law, where T_{g1} and T_{g2} represent the glass transition temperatures of the two polymers in a blend and x_1 and x_2 are the weight fraction of the individual polymers [16]. A third strategy has been to create polymer matrix composites where the matrix material was a blend developed in our lab. Roberson et al. [17] described how the key to increasing the range of applications FDM™-type additive manufacturing platforms lay in the development of new material systems. Here, three examples were given: 1) materials for electromagnetic applications; 2) materials for AM in austere, remote environments that are lacking in resources; and 3) materials for AM processes, in this case FDM™-type AM platforms. This work has served as the template for materials development in our lab.

Development of Material Systems Designed to Mitigate Problems with FDM™-type Processing

A well-known and documented detractor of FDM™ and FFF platforms is the mechanical property anisotropy of fabricated components. Particularly, the Z-direction deficiency in mechanical strength; a shortcoming well-documented in literature [18–23]. Other investigators have used post-processing steps to mitigate mechanical anisotropy such as Shaffer et al. [24], who used gamma radiation to induce crosslinking in PLA resulting in a decrease in the difference in strength between build orientations. Another path explored in literature for the reduction in mechanical property anisotropy is the development of modifications to the FFF process itself as was demonstrated by Ravi [25], who integrated a laser into a FFF platform in order to preheat the previous layer prior to deposition of a subsequent layer.
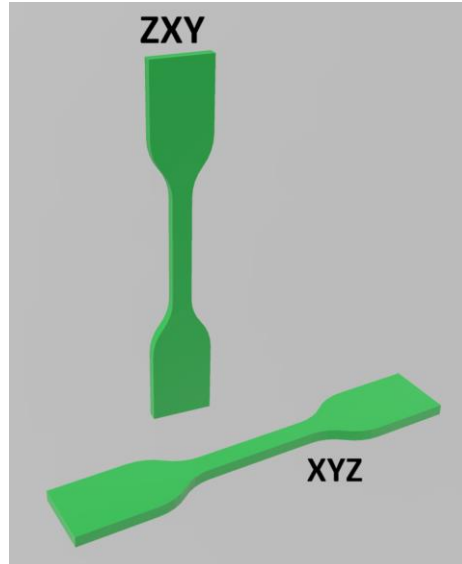
Figure 1.1 Depiction of build orientation differences.

A great bulk of the early research conducted by our group has focused on the development of materials for FDM™-type AM platforms. The premise behind this effort is creating material systems that solve a shortcoming of the FFF process or materials that benefit from the FFF process itself. The initial shortcoming we sought to solve was the Z-strength of FFF manufactured components. Works by Torrado et al. [26–27] explored the effect of several additives on mechanical property anisotropy. In many cases, the difference in strength between ZXY and XYZ (Fig. 1) oriented specimens decreased at the expense of overall mechanical strength. Here we calculate the anisotropy as a percentage difference for Ultimate Tensile Strength (UTS) by the following equation:

$$\Delta(\%)_{UTS} = \frac{UTS_{XYZ} - UTS_{ZXY}}{UTS_{XYZ}} \tag{3}$$

Many material systems were explored by the efforts of Torrado et al. [25, 26]. Most notable to mechanical property anisotropy was a ternary blend composed of three constituents: 1) ABS (grade MG37CR, Pittsfield, MA, USA); 2) the thermoplastic rubber, styrene ethylene butylene

7

styrene (SEBS, grade A1536 HU, Kraton, Houston, TX, USA); and 3) ultra-high molecular weight polyethylene (UHMWPE, GUR 1020, Celanese, Irving, TX, USA) that exhibited a decrease in mechanical property anisotropy, but at the expense of overall mechanical strength, as seen in Figure 2a. A key finding of these efforts was that obscuring the interface between print rasters (Fig. 2b) is a driving factor in the decreasing of mechanical property anisotropy, meaning that a potential path to solvency was revealed. A graphical representation of the different composites explored by Torrado et al. [26] is seen in Figure 3.
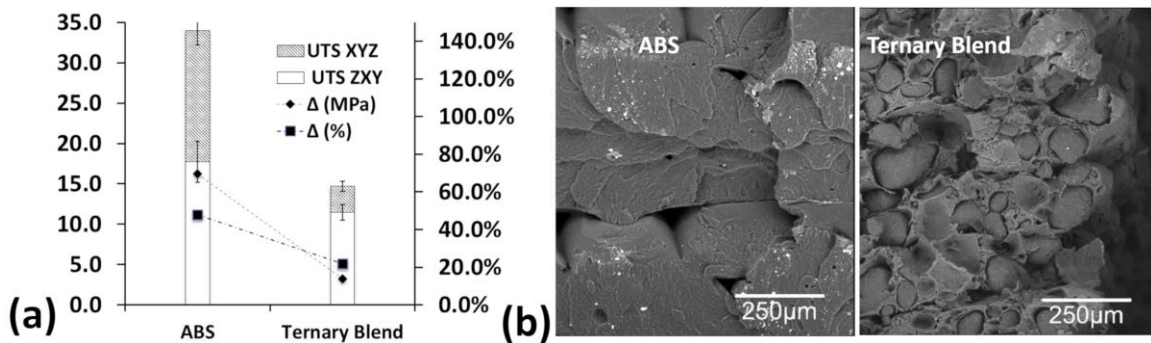
Figure 1.2 (a) Graphical representation of the anisotropy difference between ABS and a ternary blend of ABS:UHMWPE and SEBS. The UTS in for XYZ oriented specimens is represented by the shaded bar, the UTS of the ZXY oriented specimens is represented by the white bar. Anisotropy difference in terms of MPa and % difference is represented by a diamond and square respectively; and (b) examples of the differences in morphology. Data from [26].
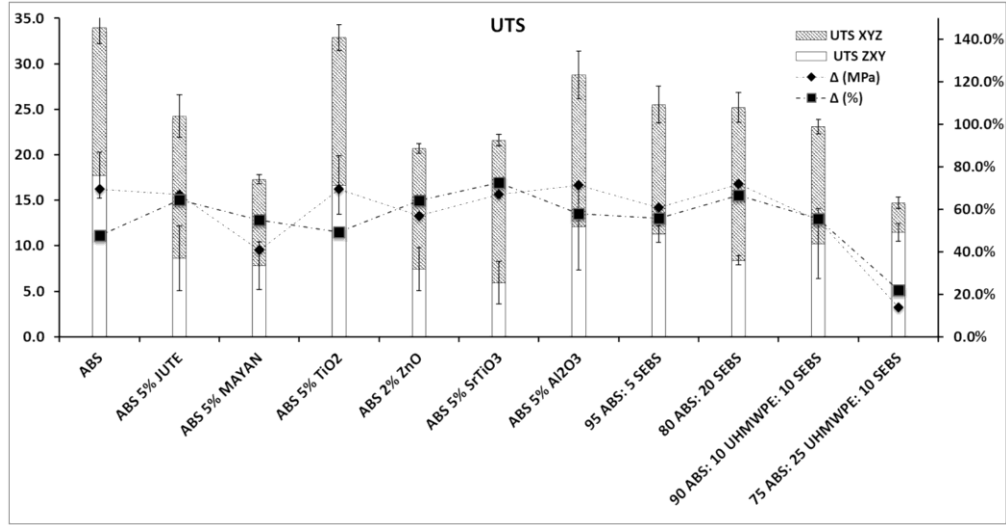
Figure 1.3 Graphical representation of the material systems explored by our group and the effect on mechanical property anisotropy. The UTS in for XYZ oriented specimens is represented by the shaded bar, the UTS of the ZXY oriented specimens is represented by the white bar. Anisotropy difference in terms of MPa and % difference is represented by a diamond and square respectively. Data from [26].

Additional work on the ABS/SEBS/UHMWPE ternary blend system as well as a binary blend of ABS and SEBS was performed by Rocha et al. [28] and serves as another example of an attempt to mitigate another shortcoming of FDM™-type AM platforms; surface finish. Particular to the rubberized blend of ABS and SEBS with a 50/50 by weight % composition, it was found that, as compared to ABS, the roughness of printed inclines (as determined by Ra value) was smoother at angles of 30° and 45° (Fig. 4a). Analysis via SEM indicated the rheology of the rubberized blend altered the way the material deposited, particularly at the edge of a specimen (Fig. 4b).

9
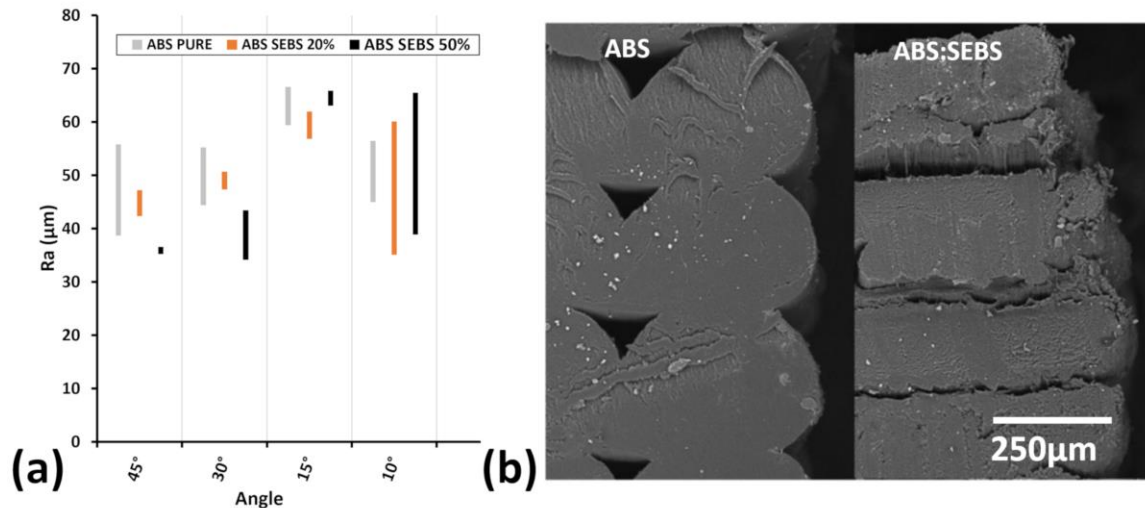
Figure 1.4 (a) Graphical representation of surface roughness measurements indicating that the addition of SEBS to ABS allowed for the printing of smoother inclined planes, and (b) SEM micrographs of ABS compared to ABS:SEBS in a 50:50 weight ratio exhibiting rheological differences between the two materials. Data from [27].

LESSONS LEARNED

These initial research efforts performed by our group came with a steep learning curve. In terms of equipment used, as mentioned above, our extruder system is equipped with a melt pump. We have found this to be invaluable in controlling filament diameter. The compounding of composites is not as simple as adding a filler to a matrix, as the constituents must be compatible with one another. Two strategies that can be taken to improve the compatibility between matrix and filler material are:1) modify the matrix; or 2) modify the filler. In the early works performed by our group, we admittedly did not have a firm understanding of these mechanisms, so no chemical modification of either the filler or the matrix was made, which is probably why, in most cases referenced above, there was a detraction in the tensile properties of the material systems. We have since developed and implemented filler functionalization processes involving silanes as well as adopted the use of matrix materials with maleic anhydride grafting to improve compatibility of matrix materials.

Development of Rubberized Blends

Ninjaflex (NinjaTek, Mannheim, PA, USA) is perhaps the gold standard for FFF-compatible thermoplastic elastomers, however, this material was not originally developed for AM technologies, rather it was repurposed from a material originally developed and used to manufacture automated teller machine (ATM) drive belts [29]. Efforts in the creation for soft elastomeric materials for FFF processes are ongoing and an early effort in the integration of elastomeric materials into FDM™ manufacturing was performed by Elkins et al. [30], who noted that the FDM 1600 system used in their effort required modification to compensate for the lack of stiffness of the elastomeric material used (the material was not specified). More recent work in the area of developing new elastomeric materials for FFF processes was carried out by Schimpf et al. [31], who synthesized a semicrystalline polyhydroxyurethane (PHU) and demonstrated compatibility with a FFF platform. Another work in the synthesis of a thermoplastic urethane (TPU) material was carried out by Harynska et al. [32], who synthesized a polycaprolactone (PCL) based polyurethane and demonstrated the manufacturing of a filament intended for FFF processes.
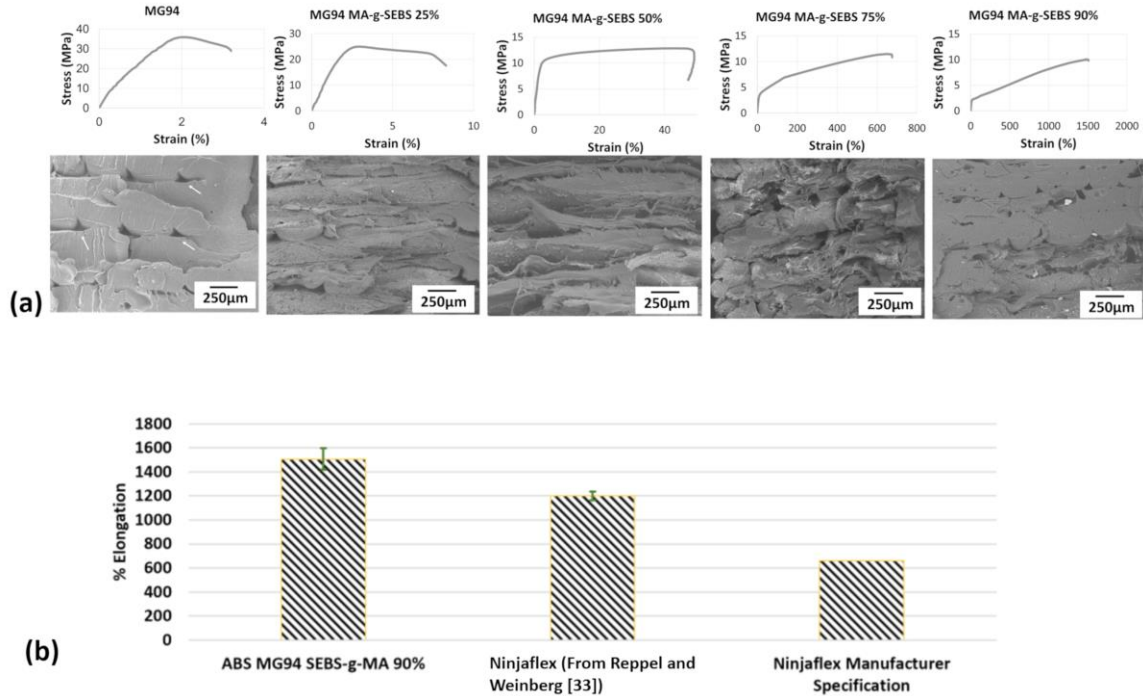
Figure 1.5 (a) Stress strain curves for the highest performing ABS:SEBS blend system studied by Siqueiros et al. [32] with representative SEM micrographs of the fracture surfaces. (b) %elongation values of the ABS:SEBS 10:90 system compared with manufacturer and laboratory published values for NinjaFlex [33].

Our work differs from others in academia as we have not utilized TPU, but rather we have used the copolymer triblock material SEBS. Work carried out by our group in the area of elastomeric materials for FFF processes stemmed from the rubberizing of ABS through the addition of SEBS via melt compounding in the afore-mentioned efforts by Torrado et al. and Rocha et al. [26, 27]. The rubberizing of ABS was further explored by Siqueiros et al. [33], however, we note that the SEBS used had been grafted with maleic anhydride (SEBS-g-MA, grade FG1901-GT, Kraton, Houston, TX, USA). The SEBS contained roughly 2% by weight maleic anhydride and we chose this material with the intent of increasing compatibility between ABS and SEBS. Additionally, two grades of ABS were compared (MG47 and MG94, both supplied from SABIC). We also note here that the grade of ABS used in prior studies by Torrado et al. [26–27] (MG37CR)

12

was discontinued. Additionally, MG94 is the grade of ABS utilized by MakerBot Industries. The key result of this work was the development of a blend composed of 90% SEBS and 10% ABS grade MG94 that was compatible with a standard desktop-grade FFF printer. Additively manufactured tensile test specimens composed of this particular blend exhibited % elongation values of 1506.6 ± 90.1%, a value we believe to be the highest recorded for an FFF material. Figure 5 summarizes the key aspects of Siqueiros et al. [33] (5a) and also compares our elongation results with the work of Reppel and Weinberg [34], who performed research on NinjaFlex (Fig 5b).
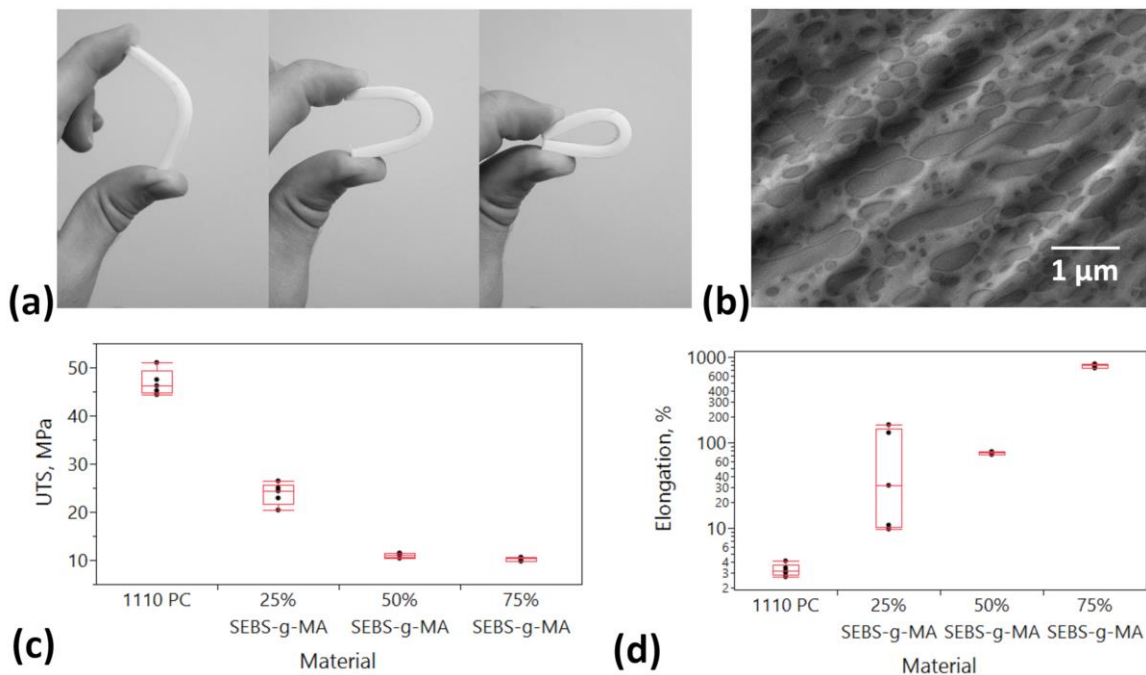
Figure 1.6 (a) PC-SEBS blend presented in Roberson and Siqueiros [36]. (b) TEM micrograph of PC blended with SEBS in a 50:50 by weight ratio. (c) UTS as a function of rubber content and (d) % elongation as a function of rubber content. Data From [36].

Further work in the rubberization of polymers was carried out by Roberson and Siqueiros [35] who demonstrated a FFF-compatible blend system composed of polycarbonate (PC, grade HF1110, SABIC, Pittsfield, MA, USA) and SEBS-g-MA. As was the case with combining ABS with SEBS-g-MA, blending PC with SEBS-g-MA yielded a material system with the ability to

sustain greater % elongation values with an increase in rubber content (Fig 6). Additionally, TEM characterization revealed a two-phase mixture, indicating the blends were immiscible (Fig. 6b). However, this blend was only partially immiscible. The morphology of SEBS is composed of a two-phase mixture, where styrene spheroids are dispersed orderly within an ethylene butylene matrix. From the micrograph of the PC/SEBS blend, it can be seen that the styrene spheroids have dissolved within the PC leaving only the ethylene butylene phase discernable.

LESSONS LEARNED

An aspect we learned from the rubberization of relatively hard thermoplastics such as ABS and PC was that to improve blending, the non-elastomeric resin should be a low molecular weight. In Siqueiros et al. [32] it was noted that blends based on the MG94 grade of ABS exhibited superior mechanical properties as compared to blends based on MG47 at the same weight percentages of SEBS-g-MA addition because of the lower molecular weight of the MG94 allowed for more robust blending. Based on this learning, when we moved on to compounding PC-based blends, we chose PC grade HF1110, as it is the lowest molecular weight PC offered by SABIC. Additionally, we found that FFF printers with direct drive style print heads as employed by LulzBot were able to reliably fabricate specimens from soft materials as compared printers with Bowden-type print heads such as the Rostock Max.

Shape Memory Polymers

When integrated with AM platforms, shape memory polymers allow for what many have referred to as "4D Printing." This leads to further enhancement the field of AM. Specific to FFF processes, most work found in literature has dealt with TPUs and polyurethane-containing blends. For example, Yang et al. [36] demonstrated the FFF compatibility of DiAPLEX, a TPU with shape memory properties, and demonstrated the printing of thermally activated grippers and a flower that

folded upon heating above the T_g. DiAPLEX is manufactured by SMP Technologies, Inc., a company that specializes in shape memory polymers. Another work involving TPU supplied by SMP Technologies, Inc. was carried out by Raasch et al. [37], who also explored the effect of thermal annealing on the mechanical and shape memory properties.
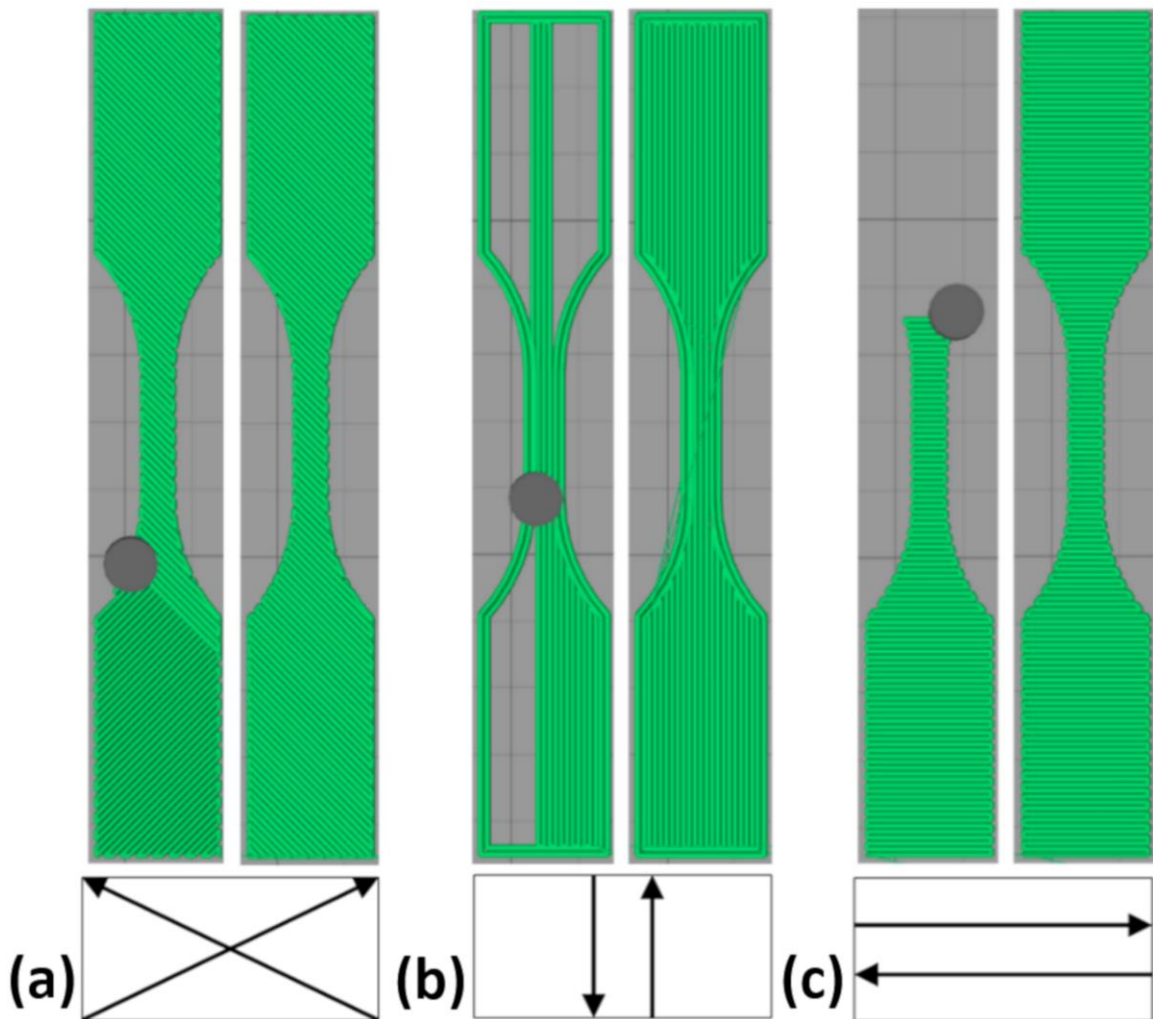
Figure 1.7 Depictions of the three raster patterns used in the shape memory polymer study by Andrade Chávez et al. [37]: (a) crosshatched ±45°, (b) longitudinal 0°, (c) transversal, 90°.

Work carried out in our group in the area of shape memory polymer development differs from what is found elsewhere in literature, as we did not rely on materials marketed to have shape memory properties. Rather, we sought to explore whether or not the rubberized blends created in

our lab possessed shape memory characteristics. Experimentation with samples composed of the 25:75 weight ratio of ABS:SEBS-g-MA revealed that this material system possessed shape memory characteristics. The effort performed by Andrade Chávez et al. [38] was a full characterization of the shape memory properties of the 25:75 and 50:50 compositions of ABS:SEBS-g-MA. Experiments were carried out at three deformation temperature regimes: 1) low temperature deformation at -40 °C; 2) room temperature deformation; and 3) an elevated deformation temperature of 105 °C for the 50:50 blend and 110 °C for the 25:75 blend, as these temperatures were near, but below the glass transition temperatures of each blend as determined by dynamic mechanical analysis (DMA). This work also provided the opportunity to examine the effect of raster pattern on the shape memory characteristics, namely, the shape fixation ratio (R_f) and shape recovery ratio (R_r). In general, these two parameters are determined by deforming a test specimen in tension to a discrete % elongation (usually 100%) and then recovering the specimen to the original shape after the application of a stimulus (in this case heat) and performing calculations based on following equations:

$$R_f(\%) = \frac{\varepsilon_u}{\varepsilon_m} \times 100\% \tag{4}$$

$$R_r(\%) = \frac{\varepsilon_m - \varepsilon_p}{\varepsilon_m} \times 100\% \tag{5}$$

where ε_u is the elongation of the specimen after the load is removed, ε_m is the maximum strain the specimen is subjected to, and ε_p is the elongation of the specimen after recovery. In this case, the specimens were printed in geometries according to the ASTM D638 standards. Here, we used three raster patterns (Fig. 7), crosshatched, longitudinal, and, transversal, where the transversal

was meant to mimic the performance of specimens printed in the Z-direction (ZXY orientation) as shown by Torrado and Roberson [39].
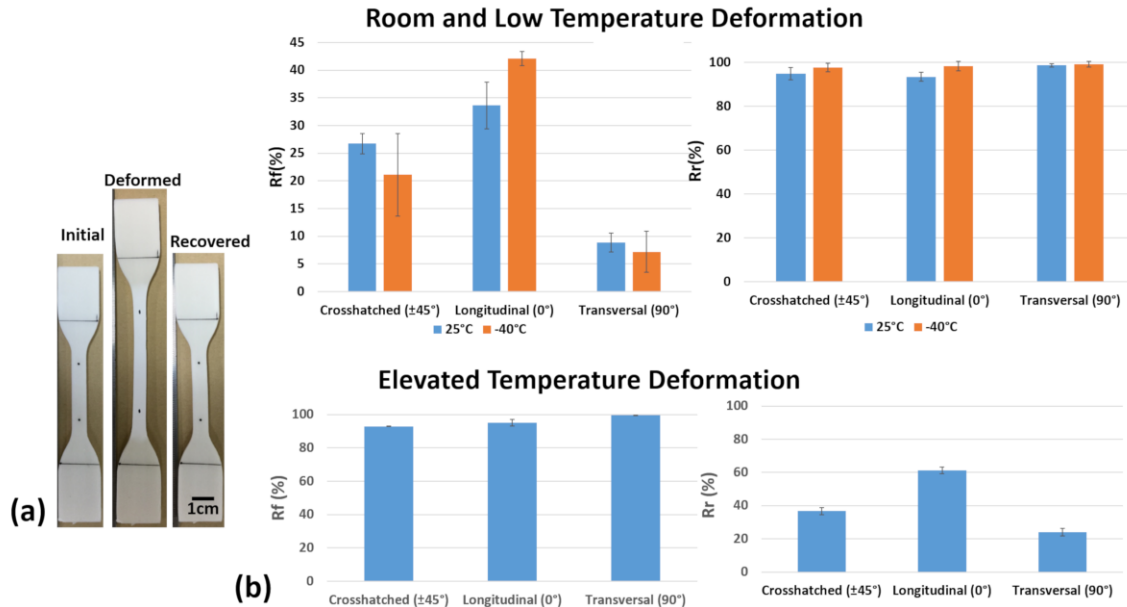
Figure 1.8 (a) Example of the shape memory characterization of the ABS:SEBS-g-MA blend and (b) data indicating the dependence of shape memory parameters on raster pattern switched between R_r and R_f depending on the deformation temperature regime for the 25:75 ABS:SEBS-g-MA blend. Data from [37].

Key findings from this effort were that there was a dependence of shape memory parameters on raster pattern. However, we also noted a relationship with deformation temperature regime. At room and low temperature deformation, the R_f, (the ability to hold a temporary shape) was dependent on raster pattern, where the longitudinal raster pattern exhibited the greatest value. At elevated temperatures, the R_r (the ability to return to the original shape) was the parameter that exhibited a dependence on raster pattern, and again, the longitudinal raster pattern exhibited the highest values. The highlights of this effort are depicted in Figure 8 and micrographs related to the polymer phase characterization will be elaborated upon below.

Electron microscopy has been an invaluable tool in the materials characterization efforts carried out by our lab. In the characterization of the shape memory polymer blends, phase characterization via scanning transmission electron microscopy (STEM) allowed us to determine that the phases within the polymer blends were aligned by the printing process, as there was a difference between specimens extracted from as-extruded filaments (Fig 9a) and as-printed specimens (Fig. 9b). Specimens were prepared by cryo-ultramicrotomy and comparing samples extracted from the as-extruded filament with a printed specimen revealed that the phases became elongated and arranged in a direction coincident with the print raster direction (indicated by the white arrow in Fig 8b.). The discernable phases also indicated that the blend was an immiscible blend. Here we see globules of ABS (the lighter phase) with the butadiene spheres (the black round features) in the center and individual styrene spheroids (white circular features) distributed within an ethylene butylene matrix. It is believed that phase alignment was caused by the FFF process and not the extrusion process because the diameter of print nozzle orifice is smaller than the extruder die orifice (~0.5mm as compared to 3.0mm).
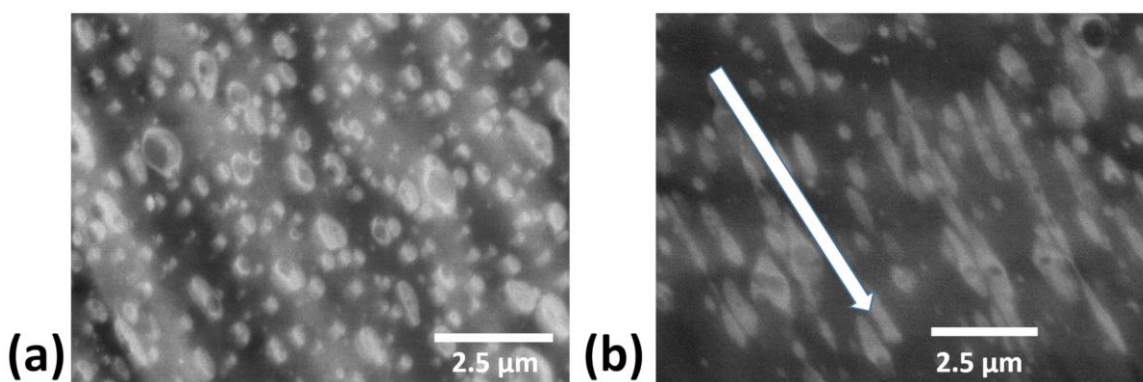
Figure 1.9 (a) STEM micrograph of an as-extruded sample of ABS:SEBS-g-MA 25:75 indicating that the blend was immiscible. The as printed specimen in (b) indicates that the FFF process elongates and aligns the phases The white arrow in (b) indicates print direction.

The most recent efforts in our group in the area of shape memory polymeric materials development have centered around the rubberization of PLA with both SEBS-g-MA and TPU (Ninjaflex). In this effort we have incorporated TPU to compare the performance with SEBS-g-MA. On its own, PLA exhibits shape memory properties that can be realized by heating the material to just below the T_g deforming to a temporary shape, allowing the object to cool, and then heating up to, or slightly above, the T_g to recover the shape [40]. An example of this is seen in the additively manufactured zig-zag structure in Figure 10. The as-printed state is the permanent shape of the structure. The zig-zag structure was heated above the T_g (~70 °C), deformed (compressed), and then allowed to cool. The original shape was recovered after, again, heating above the T_g. Based on our experience with combining ABS with SEBS to realize shape memory properties we sought to modify the pre-existing shape memory properties found in PLA. The mechanism driving the shape memory effect in PLA is referred to as "dual-state." Here, the crosslink type and strength are the components responsible for driving the shape memory process [39]. Additionally, we also sought to explore whether room temperature deformation would be possible, as PLA alone necessitates heating prior to deforming to the temporary shape. Initial work reported by Quiñonez et al. [29] entailed the blending of PLA with SEBS-g-MA at percentages of 5%, 10%, 25%, and 50%. All weight percentage blends were compatible with a standard FFF printer. Printed Izod impact test specimens exhibited an increase in impact strength with the addition of 5% SEBS-g-MA, however, unexpectedly, the impact strength lowered at the 10% increment and then exhibited a dramatic increase for loadings of 25% and 50% by weight SEBS-g-MA. SEM microanalysis of the fracture surfaces of the impact specimens composed of the blend compositions indicated that the fracture behavior became more ductile with an increase in rubber content (Fig. 11), to the point that the individual print rasters exhibited necking for the 50:50 composition. Additional features

19

of the brittle fracture mode are the craze cracks indicated by the white arrow in Fig. 11a. The white

arrows in 11c and 11d, are pointing out fibrils, another indicator of a ductile failure mode.
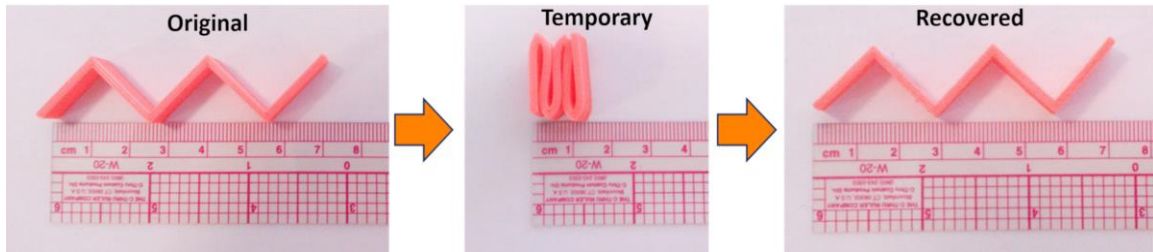
Figure 1.10 Demonstration of the shape memory properties of a PLA structure made by FFF.

Analysis via DMA showed a decrease in max tan δ, but the dampening response after the

glass transition temperature peak was roughly the same, meaning that the rheological behavior

after the glass transition temperature was the same for all the blends. Further work by Quiñonez

[41] incorporated TPU in the same weight percentages as the SEBS-g-MA in order to act as a

comparison. It was found that the addition of TPU yielded a similar impact resistance behavior as

was observed when adding SEBS-g-MA in that there was a slight dip at 10% by weight and then

a dramatic increase at the 25 and 50% iterations. However, the addition of TPU yielded higher

impact resistance values as compared to SEBS-g-MA at these weight ratios. The impact test data

for this effort is tabularized in Table 1.
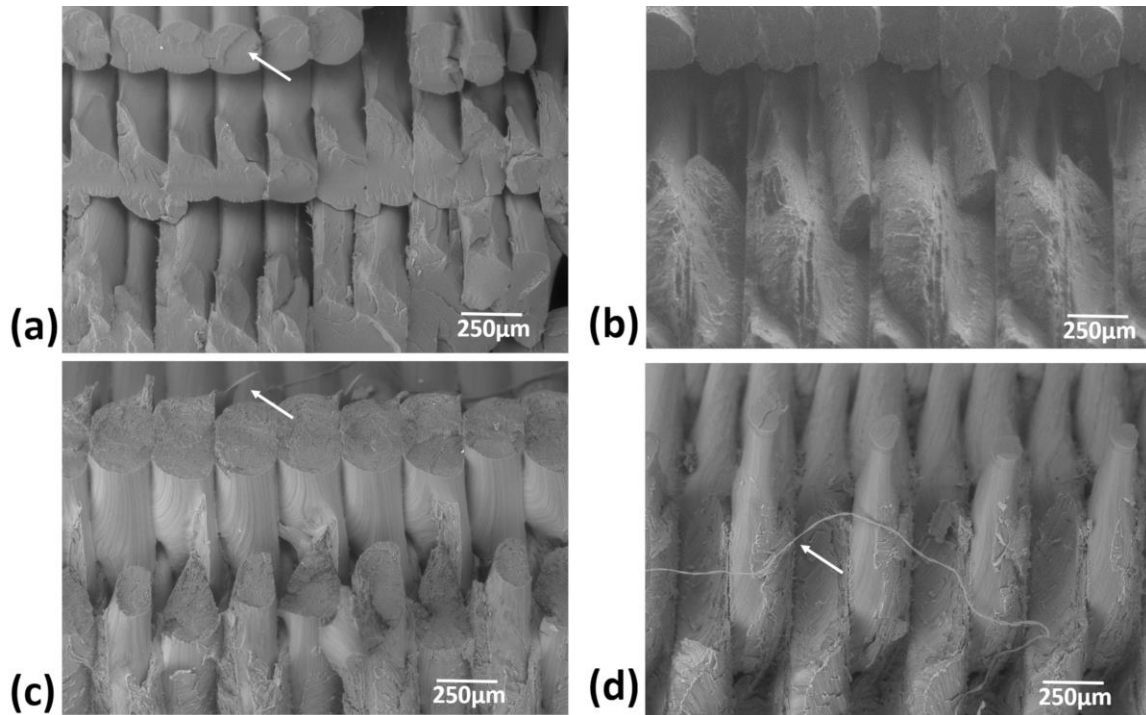
Figure 1.11 SEM micrographs of spent Izod impact test specimens where (a) is PLA loaded with 5% SEBS-g-MA, and (b), (c), and (d) correspond to rubber loadings of 10, 25, and 50%, respectively. Note the transition in fracture surface morphology from brittle to ductile as rubber content increased. Data from [28].

Initial characterization of the shape memory performance is seen in Figure 12 for 75:25 ABS:SEBS-g-MA blend. Room temperature deformation led to necking of the specimen, which could be considered damage. The specimen recovered to nearly its original shape upon exposure to 80 °C in an oven for 5 min. In terms of calculated shape memory performance, the R_r and R_f values were 97% and 88% respectively. Further characterization of both blend systems at higher elastomeric content indicated that there was an increase in additively manufactured components shape memory performance values in the longitudinal raster pattern as compared to injection molded specimens. This comparison of AM to a more traditional manufacturing method (injection molding) further supports the hypothesis that phase alignment improves shape memory performance as was alluded to in the previously mentioned shape memory polymer development

21

effort conducted by Chavez et al. [38]. Our lab's efforts in the area of shape memory polymer development serve as another example of the development of material systems whose physical properties can benefit from the AM processing to which it is subjected. Further study of this material system is warranted and is one of the many aspects that lay ahead in the area of novel material development.
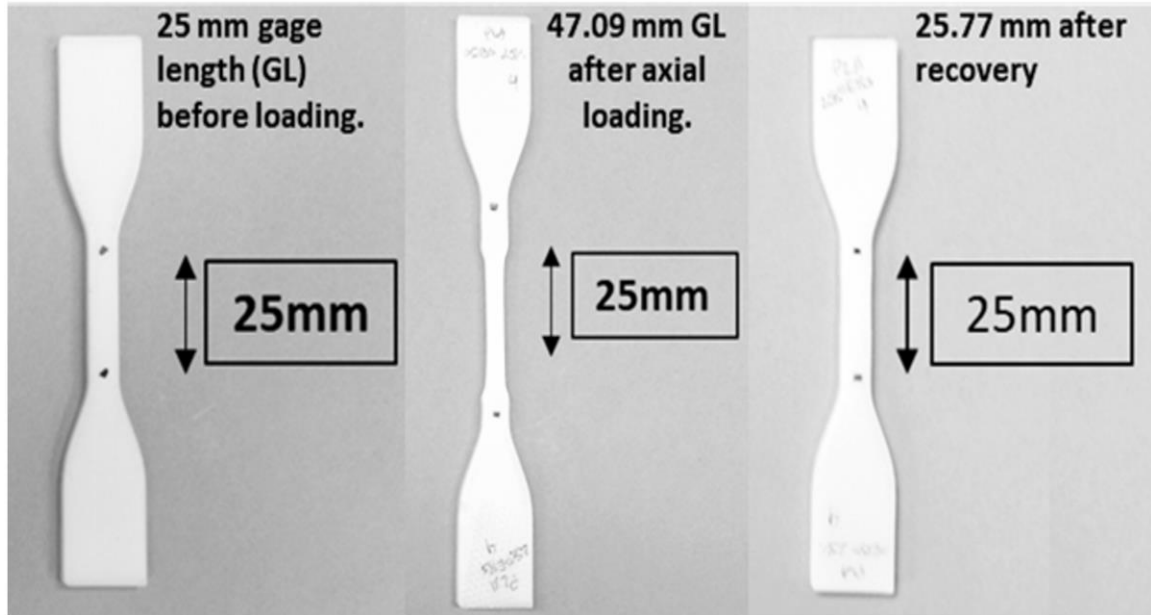
Figure 1.12 Initial shape memory characterization of the PLA:SEBS-g-MA blend at the 75:25 composition. Data from [28].

TABLE 1.1 TABULARIZED IMPACT RESISTANCE DATA OF ADDITIVELY MANUFACTURED IZOD IMPACT TEST SPECIMENS FOR THE PLA/ELASTOMER SYSTEMS. DATA FROM [40].

Wt. % Elastomer	Impact Strength, J/m (PLA:TPU)		Impact Resistance, J/m (PLA:SEBS-g-MA)	
	AVG	STDEV	AVG	STDEV
0%	30	0.5	30	0.5
5%	58	0.9	49	8.8
10%	34	11.5	45	11.8
25%	95	13.12	58	39.9
50%	381	19.2	201	67.6

The incorporation of a soft elastomeric constituent in a thermoplastic blend enables the shape memory mechanism of dual-component. Here, the driving force for the shape memory process is the presence of physically hard and soft domains [39]. In the case of ABS, which has no significant shape memory characteristics on its own, shape memory properties were enabled by the incorporation of the thermoplastic rubber, SEBS. In the case of PLA, the shape memory mechanism was switched from dual-state to dual-component, which also enabled deformation of the material at room temperature. While, in most cases, shape memory properties are characterized by elevated temperature deformation, our work shows that exploration of other deformation temperature ranges (room and below) uncovers aspects related to the shape memory process that would not otherwise be realized. Finally, the ability to align phase domains trough the FFF process allows for discrete control over the shape memory properties for dual-component SMP material systems.

Electromagnetic Materials Development

The range of materials developed for the use of FFF in electromagnetic applications literature is broad. An example is the development of electrically conductive ABS for electromagnetic interference (EMI) shielding by Schmitz, et al. [42], where ABS was loaded with carbon nanotubes and carbon black to increase the electrical conductivity. An example of the creation of FFF-compatible dielectric materials was demonstrated by Khatari et al. [8], who, as mentioned earlier, created an ABS-based system with tunable dielectric properties by compounding the terpolymer with varying weight percentages of barium titanate.

A key effort in the area of electromagnetic materials performed by our lab was the creation of a PC (Lexan FXD171R, SABIC, Pittsfield, MA, USA) matrix composite filled with tungsten

particles made for the application of radiation shielding reported by Shemelya et al. [43]. Here, a functionalization process to modify the tungsten particles was used, which entailed the silanization of the tungsten particles in order to promote adhesion between filler and matrix. Composites were created with 1%, 3%, and 5% by weight tungsten and exhibited an increase in stiffness (as determined by DMA) corresponding with the increase in tungsten content. The amount of X-Ray radiation passed through test specimens decreased with an increase in tungsten content meaning that the attenuation factor of the material system was tunable. The design of this material was carried out according to the Beer-Lambert law [44]:

$$I_x = I_o e^{-\left(\frac{\mu}{\rho}\right)_m \rho_m x} \tag{6}$$

where $\left(\frac{\mu}{\rho}\right)_m$ is the mass absorption coefficient of the mixture, x is the length of the sample, ρ_m is the density of the mixture, I_x is the intensity of radiation after the X-Rays have passed through the material and I_o is the initial intensity of the radiation. Both the mass absorption coefficient of the mixture and the density of the mixture were calculated from two law of averages-type equations based on the weight percentage of each constituent (signified by x_1 and x_2), in this case tungsten and polycarbonate:

$$\left(\frac{\mu}{\rho}\right)_m = x_1 \left(\frac{\mu}{\rho}\right)_1 + x_2 \left(\frac{\mu}{\rho}\right)_2 , \tag{7}$$

where $\left(\frac{\mu}{\rho}\right)_1$ and $\left(\frac{\mu}{\rho}\right)_2$ are the mass absorption coefficients of the individual constituents, 1 and 2, and

$$\rho_c = x_1 \rho_1 + x_2 \rho_2 , \tag{8}$$

where ρ_1 and ρ_2 are the densities of constituent 1 and 2, respectively. Since no alloying or lattice parameter change was expected to occur in the combining of tungsten with PC, it was determined safe to assume this methodology for composite density. Experimental results confirmed the predicted model of attenuation factor for the four materials studied in this effort. The decrease in radiation passed-through corresponding with an increase in tungsten content along with an example of printed specimens can be seen in Figure 13.
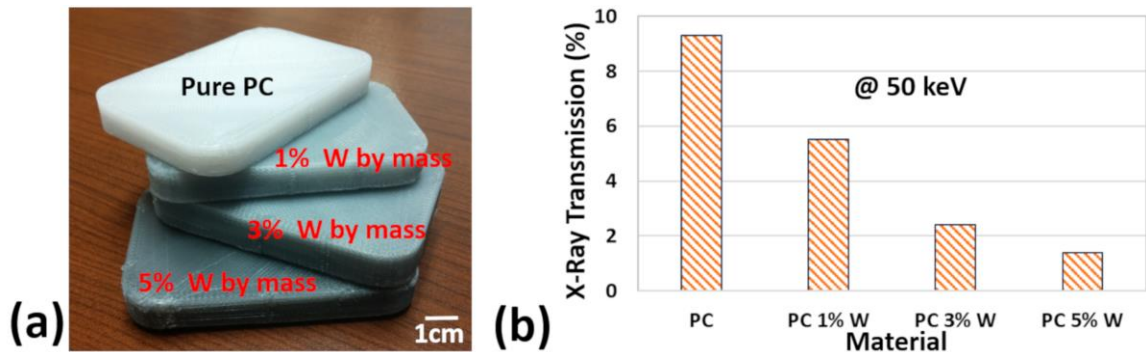
Figure 1.13 (a) Radiation shield specimens composed of pure PC and three tungsten loadings that were made by way of FDM™. The graph in (b) indicates the percent of X-Rays transmitted through the specimens where the beam energy was 50 keV. Data from [42].

LESSONS LEARNED

In this work, we began developing and incorporating silane functionalization processes that were applied to the filler material prior to combining with the polymer matrix material in order to promote dispersion within and adhesion to the polymer matrix. A notable result of this was that there was an increase in the impact strength with an increase in tungsten content. In this work we found it useful to normalize the mechanical testing data based on specific gravity measurements to gain insight into the actual strength of the compounded materials without convolution of air gaps produced by the FDM™ process. Additionally, we found it beneficial to utilize a master batch of highly loaded PC that was then diluted in the melt compounder to the desired weight percentage by combining granulate of the highly loaded material with neat PC.

Sustainable Materials Development

There are two main categories in the area of sustainable materials for FFF processing: 1) the development of biodegradable/bio-based materials; and 2) recycling waste streams into useable feedstock for FFF processing [45]. Examples in literature of the use of biodegradable materials for FFF processing mainly involve PCL and PLA [46–47]. Notable works in the area of repurposing waste material into FFF feedstock material were demonstrated by Zander et al., who created feedstock materials and composites from recycled polyethylene terephthalate (PET) water bottles and polypropylene packaging [48–49].
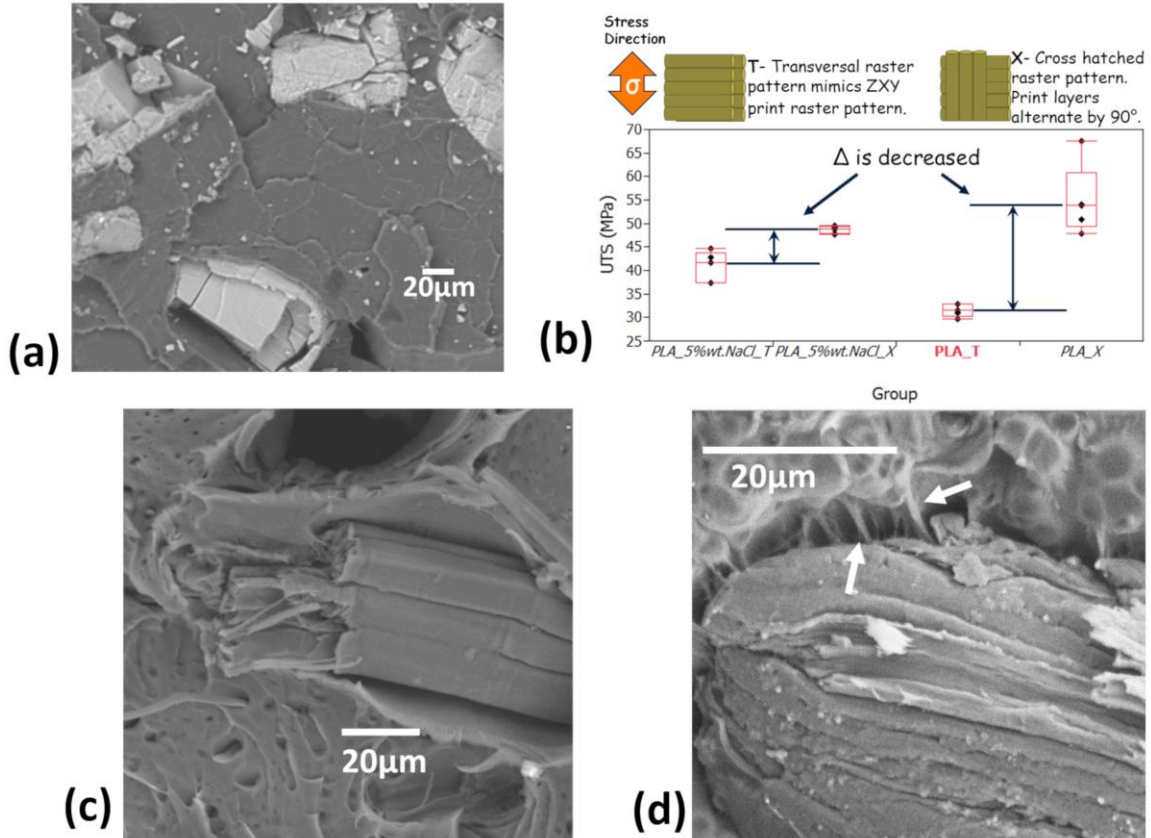
Figure 1.14 (a) SEM micrograph of the composite of PLA combined with NaCl at 5% by weight. (b) Box plots comparing tensile specimens of two different raster patterns, where the composite of PLA filled with NaCl exhibited a lower mechanical property sensitivity to raster pattern. The SEM micrograph in (c) is of non-functionalized jute plant fiber combined with PLA note the poor interface between fiber and matrix. The SEM micrograph in (d) is of jute plant fiber that was functionalized by first soaking the fibers in supersaturated NaCl solution. Note the fibrils highlighted by white arrows. Data from [50].

Efforts in our lab in the area of sustainable materials for FFF-type additive manufacturing initially centered around the improvement of the engineering properties of PLA, as this thermoplastic is sourced from renewable resources such as corn and is compostable [50]. Another work conducted by Rocha [51] centered upon the development of several PLA matrix FFF-compatible composite systems. For this effort, we used PLA Grade 4043D, (NatureWorks, Minnetonka, MN, USA) a grade supplied in filament form by many FFF filament manufacturers. One of the goals of this effort was to find sustainable modifiers that would enhance the filler/matrix interface to act as an alternative to more toxic chemicals such as the afore mentioned silanes. It was found that combining PLA with NaCl (Fig. 14a)—commonly referred to as table salt, but in this case, a reagent grade chemical (halite) was used—decreased the raster pattern sensitivity of printed tensile test specimens (Fig. 14b). SEM microanalysis revealed the interface between NaCl and PLA to be robust, making it a potential candidate to utilize as a functionalization treatment. Jute plant fiber was treated with supersaturated aqueous solutions of NaCl and the result was a difference in the adhesion between fiber and matrix as evident by the presence of fibrils between the matrix and fiber on spent tensile specimens (Fig. 14d) that were not observable when no functionalization was used (Fig 14c).

Figure 1.15 Combining waste products from two streams, plastic food packaging and textiles to create an advanced FFF-compatible composite. Data from [51, 52].

Additional efforts in the area of sustainable composites have been carried out by our group where the focus has been on the use of recycled or upcycled materials. One example was carried out by Carrete et al. [52] and Carrete [53], who created a cotton-fiber reinforced PET composite, where the PET was created from recycled water bottles and the cotton fibers were sourced from denim. Here the cotton fibers were subjected to an acid hydrolysis treatment to remove the amorphous region of the fiber, leading to the separation of cellulose crystalline particles that were then filtered and subjected to a silane functionalization process. An example of the crystalline fiber is seen in the SEM micrograph in Figure 15. Both the recycled PET and PET/cellulose composite were able to be printed with a standard FFF printer. Analysis via DMA of printed specimens indicated that the max tan δ was increased due to the addition of the crystals at 10% by weight from 0.28 to 1.32 meaning that the energy dissipating capability of the material was increased. Impact testing was carried out on additively manufactured impact test specimens, which exhibited an increase in impact resistance from 14.38 ± 2.579 J/m for the PET to 23.3 ± 5.210 J/m for the PET/cellulose composite. This work was an example of utilizing the AM process of FFF as an outlet for two waste streams: 1) polymeric waste; and 2) textile waste; while also serving as a template for the creation of feedstock materials in austere, remote environments where neat polymer sources may be in short supply or hard to acquire.

The decrease in anisotropy due to the addition of NaCl to PLA is an aspect that warrants more investigation as it implies that the solvency of a great detractor to FFF manufacturing processes could be mitigated by the addition of an abundant mineral. A difficulty encountered in work with recycled bottles was granulating the water bottles. A combination of a Filabot Reclaimer and paper shredder was used and the process was not as straight forward as feeding a whole bottle to either shredding tool. Additionally, extracting cotton fibers from denim material was tedious as it was carried out by hand. When combining the hydrolyzed filler material with the PET granulate, a drastic drop in viscosity occurred, presumably caused by a hygroscopic response by the PET matrix [51]. For the PET material system, we found it necessary to employ air cooling during the extrusion process, as water cooling of the extruded filament caused coiling due to rapid crystallization. Both PLA and PET are polyesters that exhibit hygroscopic behavior, so we had to dry the filaments prior to printing specimens.

Development of Hybrid Material Systems

Hybrid material systems have also been explored by our group, where the term "hybrid" refers to creating a composite where the filler material has a similar T_g to the matrix material. The expectation was that the filler material would not be in a solid state during the melt compounding and/or FFF manufacturing due to the processing temperatures. We are not aware of other investigators who have conducted research in this area. The drive for this effort was to understand if the morphology of the filler material could be influenced by the FFF processing. We expected the filler to change from the original morphology into that of drawn wires. To relate back to the original template that we have followed in our lab, this branch of research falls into the category of developing materials for FDM™-type processes. One effort in this area was reported by

Siqueiros and Roberson [54] who synthesized a tin fluorophosphate glass (P-glass) with a relatively low T_g (compared to SiO_2 at 1300 °C) originally reported elsewhere to be in the range of ~110 °C [55]. Considering that the temperature ranges of the extrusion and FFF processes are over 200 °C, it was expected that the morphology of the filler material would change during either process. The initial morphology of the P-glass was flake like. Two different polymer matrix materials were used: 1) the 50:50 weight ratio blend of ABS MG94 and SEBS-g-MA mentioned above; and 2) PLA (Grade 4043D, NatureWorks, Minnetonka, MN, USA). Composites based on the ABS/SEBS blend were created with 5, 10, and 20% by weight P-glass. We could not achieve a printable filament of PLA loaded with 20% by weight P-glass due to filament brittleness so loadings of 2.5, 5, 10, and 15% by weight were created.

In the case of ABS:SEBS-g-MA loaded with 5% by weight P-glass, wire drawing was observed where the flakes were drawn into an elongated morphology, but an increase in mechanical properties was not realized. Moreover, it appeared as if loadings of P-glass greater than 10% by weight began to negatively affect the mechanical properties. It was then found that the amount of air gap in the loaded specimens due to the FFF process was somewhat large. The density of printed specimens decreased with an increase in P-glass loading leading to, at worst, specimens that were only ~60% dense. We came to this conclusion by comparing theoretical density measurements to actual density measurements. Normalization based on specific gravity measurements (a strategy we first employed in our work with radiation shielding material) was employed to accurately assess the effect on mechanical strength and it was found that based on normalized data, the UTS values increased for each loading, but plateaued after 10% by weight loading for the ABS:SEBS-g-MA matrix system. A similar behavior was observed in the case of the PLA matrix system. Again, it was noticed that the density of printed specimens decreased with

an increase in P-glass loading. Normalization was, again, used to determine the actual strength of the compounded material and it was found that the addition of P-glass had a beneficial effect on UTS for all loadings, but the benefit was greater at lower loadings of 2.5 and 5% by weight. At higher weight percentages, the P-glass particles begin to agglomerate. A graphical representation for the P-glass composite system is seen in Figure 16, where normalized data is compared to as-measured data.
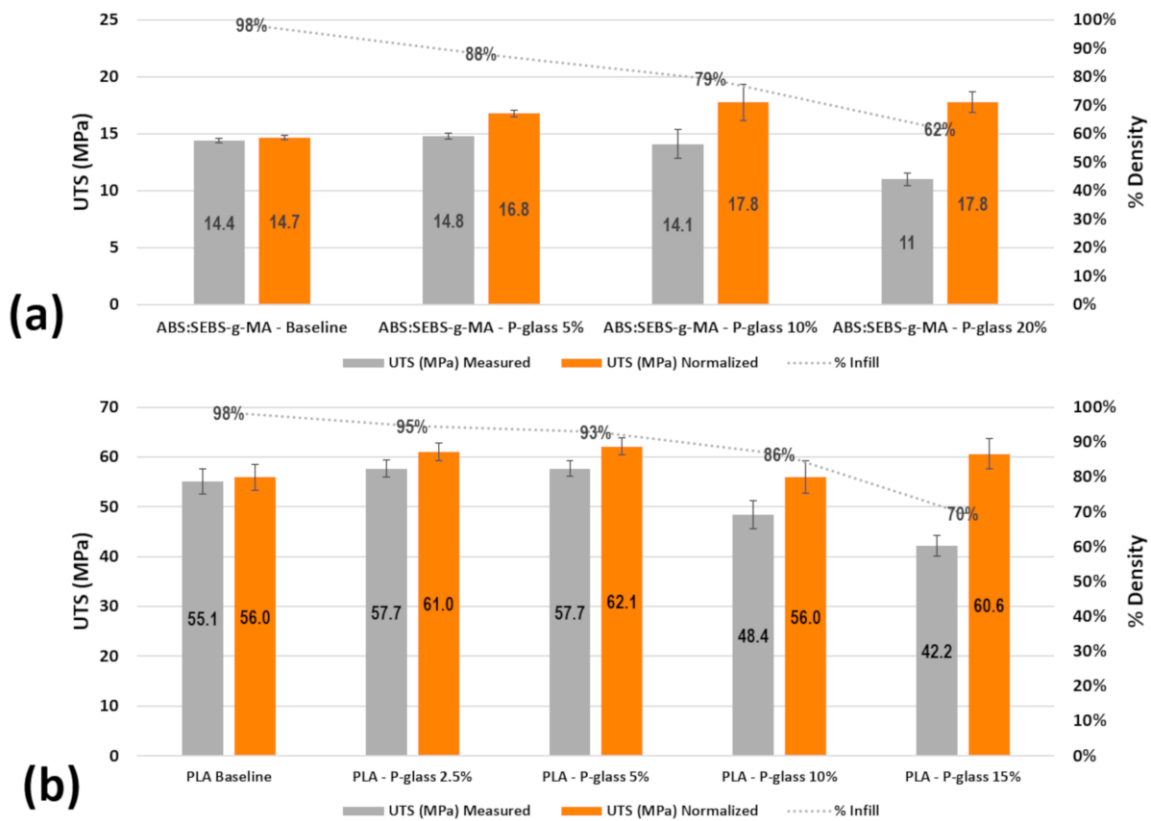
Figure 1.16 Graphical representation of UTS values for (a) ABS:SEBS-g-MA loaded with P-glass at various weight percentages and (b) PLA loaded with P-glass at various weight percentages. Note the effect of normalizing the values based on measured specimen density. Data from [53].

Further analysis of the PLA matrix version of the P-glass composite revealed a discernable sensitivity to pre-processing steps that the filament was subjected to before the printing process. It was found that the as-extruded filament exhibited sensitivity to moisture and no in situ wire

drawing was observed post printing due to a decrease in matrix viscosity. As mentioned above, we typically employ water-cooling in the extrusion process and found this to be the source of moisture. The experiments with the PLA matrix composite were repeated, for baseline PLA and PLA loaded with 10% by weight P-glass however, this time the filament was dried prior to printing tensile test specimens following the manufacturer recommended drying schedule of 4 hours at a temperature of 80 °C. When analyzing the fracture surface of spent tensile specimens, wire drawing was observed as the PLA was viscous enough to change the morphology of the glass during the printing process. An increase in UTS values was also observed when the data was not normalized, and was even more profound when the data was normalized based on specific gravity measurements. Further, it was found that increasing the print temperature to 240 °C and 260 °C (as compared to our usual temperature of 220 °C) also led to an increase in wire drawing and an increase in tensile strength values for PLA loaded with 10% by weight P-glass when the filament was dried prior to printing. We also note that the increase in strength with an increase in print temperature was also observed in the case of unfilled PLA baseline specimens. The effect of increasing print temperature on the UTS values of dried filaments is seen in Table 2.

TABLE 1.2 THE EFFECT OF INCREASING PRINT TEMPERATURE ON PLA AND PLA LOADED WITH 10% P-GLASS FOR FILAMENTS THAT WERE DRIED PRIOR TO THE PRINTING PROCESS. DATA FROM SIQUEIROS AND ROBERSON [53].

Material	Print Temp (°C)	Ultimate Tensile Stress (MPa)	ST. DEV	Normalized UTS	ST. DEV	Tensile strain at Break (%)	ST. DEV	(n)
PLA/P-glass 10%	220	57.1	2.91			3.19	1.63	3
PLA/P-glass 10%	230	56.8	0.67			2.88	0.16	3
PLA/P-glass 10%	240	58	1.74	67.7	2.2	3.34	0.42	3
PLA/P-glass 10%	260	57.5	0.85			4.67	0.62	3

PLA Baseline	220	56.4	2.18			5.29	1.46	3
PLA Baseline	230	56.2	2.22			2.98	0.63	3
PLA Baseline*	240	57.6	1.46	57.6	1.5	3.96	1.13	3
PLA Baseline	260	59.5	2.61			4.42	0.87	3

*Specific gravity measurements confirmed the PLA specimens to be 100% dense.

Another effort by our group in the area of hybrid materials development involved a metallic tin-containing filler as presented in Andrade Chávez et al. [56]. Here, eutectic SnBi spherical particles with a nominal diameter of 8.8µm were compounded with ABS, PLA, as well as three iterations of the ABS:SEBS-g-MA blend, where the rubber was added in increments of 25, 50, and 75% by weight. It was theorized that the compounding and printing processes would change the spheroid morphology of the SnBi particles to that of an elongated wire-like structure. The efficacy of silane functionalization was also of interest due to the fact that the operating temperatures of the extrusion and printing process were well above the melting temperature of the filler material.

Key results of this work were that a change in morphology of the SnBi particles was observed for every material type where the spheroid particles were drawn into wires. Agglomeration of the SnBi particles at loadings higher than 10% by weight led to a detraction of the mechanical properties. The efficacy of functionalization was evident in ABS, which exhibited an increase in tensile strength from 33.17 ± 1.12 MPa to 37.82 ± 1.76 MPa that was verified by Tukey Kramer HSD to be statistically significant. On the other hand, non-functionalized particles lessened the UTS values also by a statistically significant amount. Functionalization was also beneficial to the relatively low loading of SEBS-g-MA in the 75:25 by weight ratio of ABS:SEBS-g-MA. Silane functionalization appeared to lose efficacy as the increase in SEBS-g-MA content increased.

In the case of the composite created from PLA and SnBi, we were only successful in creating a printable filament at the loading of 5% by weight. Again, the efficacy of

functionalization was observed, but the tensile strength of the functionalized composite was only able to match that of neat PLA control specimens whereas no functionalization led to a decrease in UTS values. Fracture surface microanalysis via SEM of a specimen from the functionalized data pool revealed that the SnBi had been drawn into a rod-like shape, indicating that in-situ wire drawing had occurred.
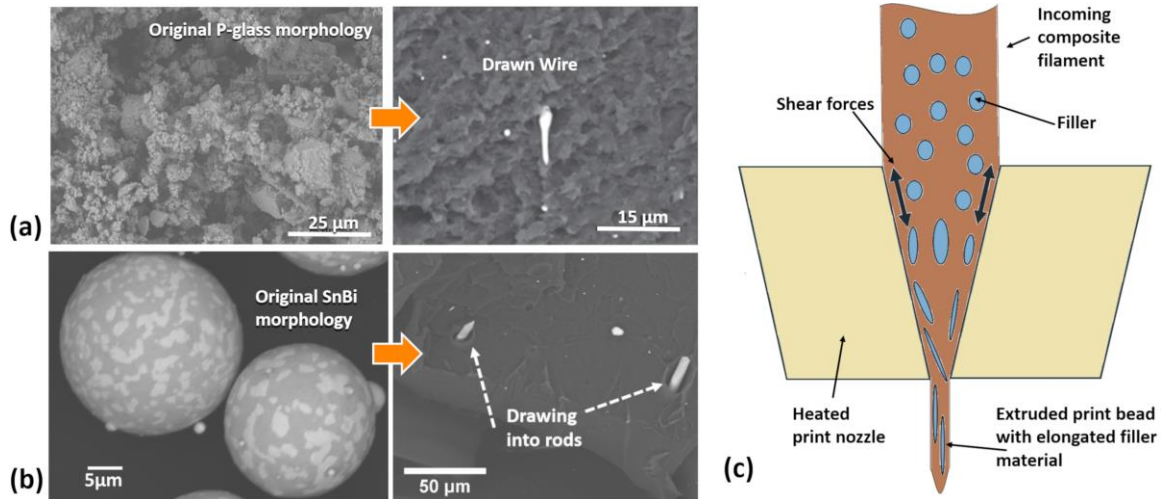
Figure 1.17 The filler materials in hybrid materials can be drawn in-situ into wires by the additive manufacturing process of FFF. (a) SEM micrograph of the original morphology of P-glass and the transition into a wire form in a specimen of 5% (by wt.) P-glass in SEBS-g-MA. (b) SEM micrograph the original spheroid morphology of SnBi particles that transform to a wire-like form in a printed specimen of 5% (by wt.) SnBi in PLA and (c) a schematic of the in-situ wire drawing process. Data for (a) and (c) from [53] and data for (b) from [55].

As mentioned above, the efforts to create hybrid material systems was aimed at utilizing the FFF process to dictate the morphology of the filler material. In both the cases of P-glass and SnBi, the printing process had a more profound effect on the morphology of the filler material as compared to the melt compounding process. As was the case with polymer phase alignment, it is believed that the printing process is the driver of wire drawing due to the relatively small orifice size of the print head nozzle compared to the extruder (~0.5mm compared to 3mm). A schematic depicting the change in morphology is shown in Figure 17c. Further work in this area should be

carried out to greater characterize the wire drawing process and to examine the relationship between raster pattern and mechanical strength.

LESSONS LEARNED

Drying of the extruded PLA filament is paramount. We have always employed a pre-extrusion drying process in a Dri-Air CFAM micro air dryer. When working with hygroscopic materials, it is paramount to incorporate drying of the filament before the printing step. In the case mentioned above, the melt flow index value for the extruded PLA was ~16 g/10 min as compared to the specified value of 6 g/10 min making the effects of moisture evident. Discrete experimentation with the printing temperature is also a necessity in the management of the in-situ wire drawing process. Again, specific gravity measurements to normalize data is a good way to enable deconvolution of the presence of air gap when trying to assess the bulk strength of a printed material. However, this process is quite tedious and in some cases is not feasible for large data sets. As mentioned above, there are two strategies for increasing compatibility between filler and matrix: altering the filler or altering the matrix. In the case of SnBi blended with a maleic anhydride containing material, it was evident that combining these strategies may not always be the best course of action.

Looking Ahead and Conclusions

With respect to our lab, the future focus entails continued research into the development of materials with properties that can benefit from the FFF printing process. An additional focus will be on the development of recycling solutions and sustainable materials that either enable their removal from the associated waste streams or a change in the behavior of polymers once they have been discarded. Efforts in understanding the effects of the FDM process on material degradation will also be a strong area of interest moving forward. We have already begun efforts to understand

this phenomena in another effort by Carrete et al. [57], who explored the degradation effects of exposing FFF manufactured PETG and PLA specimens to various liquid media by fractography of exposed tensile specimens. Failure analysis based on fracture surface characterization has been and will always be a key aspect of our research. The first work generated by our lab was a failure analysis effort of novel composites for FFF applications performed by Torrado et al. [25] and we have incorporated an aspect of fracture surface analysis in every work we have published. Future shape memory polymeric materials development includes determining if the PC-SEBS system exhibits shape memory properties. If so, this shape memory polymer system would be expected to operate at a higher temperature as compared to the ABS-SEBS system discussed above as the T_g is higher according to Fox's Law meaning that the operation temperature for shape memory is higher. Additionally, the effect of crystalline domains on degradation and shape memory mechanisms is of great interest to our lab.

   Increasing the applicability of FDM™-type AM platforms will continue to rely on a continually growing array of material systems. While the most widely used material for this AM platform continues to be ABS, the important research taking place in academic environments to create novel material systems continues to grow in significance. The activities of the Polymer Extrusion Lab (PEL) represent only one of many efforts in this area across the world. The perceived lack of materials development in the commercial sectors may simply be an indication that average user of FDM AM platforms does not require boutique material properties, like radiation shielding or those necessary for energy harvesting. However, there is the belief by our lab that this notion will change over time with the development of broadly applicable new materials.

Chapter 2: Development and Characterization of Self-Healing Polymer Blends for Additive Manufacturing

Introduction

Humankind has been making use of processed polymers for nearly 3700 years starting with Mesoamerican cultures who extracted latex from the *Castilla elastica* tree and combined it with a liquid obtained from a vine known as *Ipomoea alba*; controlling the elasticity of the resultant mixture by varying the ratio of liquid to latex [58–59]. The ancient cultures of Mesoamerica had a fundamental understanding of the materials they were dealing with and could develop different recipes based on the application, which, in the case of this rubber compound, ranged from balls for ceremonial games to bands used to manufacture tools [58]. Undoubtedly, a key enabler for the success of these cultures' mastery of polymer processing and manufacture was the understanding of material performance in a variety of conditions. The method of controlling polymer properties through composition control will be utilized by the research effort proposed here, but with the added twist of manipulation of phase texture by way of advanced manufacturing techniques.

Fast forward to modern times and humankind has an unparalleled ability to fabricate objects from a wide variety of polymers and manufacturing methods. However, now the stakes are much higher than those experienced by those early adopters of polymers from long ago, as components fabricated from polymers are expected to reliably perform in a wide variety of theatres ranging from components used in aerospace systems to those that support human life in healthcare situations to applications that are often thought of as disposable such as food packaging and trash bags. However, there are several downsides to society's use of plastics. A key detractor of the widespread use of plastics is due in part to the way they behave in the environment, particularly in

oceans and waterways. The specific gravity of most polymers is close to a value of 1, the same as water, meaning that polymer waste tends to float in water at various depths depending on the size of the plastic object [60]. Mechanical degradation causes plastic material to break down into smaller and smaller particles until they reach the microscale. These "microplastics" are ingested by fish and other wildlife and can lead to their death [61]. Chemicals such as phthalates that are commonly found in plastics disrupt the endocrine systems of fish and wildlife and negatively affect their reproductive systems, leading to a negative impact on the population of these animals [62]. The impact of microplastics is not limited to fish and other wildlife as it is estimated that the amount of microplastics ingested by consumers of seafood is on the order of 11,000 particles per year for a person [60]. This indirect consumption of endocrine harming chemicals by humans can pose a health risk as plasticizers have been linked to a wide range of endocrine-related health problems and have also been shown to negatively affect fetal development in humans [63]. While in the body, microplastics can further degrade to the nanoscale and be absorbed by body tissue leading to an immunoreaction [64]. Microplastics have now been found in every ecosystem, meaning that risk of human consumption is not limited to seafood eaters [65]. Even more disturbing is the fact that microplastics have been detected in the fecal matter of humans in several studies [64–67] and has been linked with Inflammatory Bowel Disease in humans [66]. Perhaps the most shocking discovery related to the impact of polymeric materials on humans is the detection of microplastics in the blood and tissue of human placentas [68] as well as human whole blood tested from samples obtained from random blood donors [69]. Furthermore, microplastics have been found in the lung tissue of living human beings [70] meaning that plastic waste is literally in the air we breathe!. How we handle plastic waste is a big problem. Today plastic refuse can be found on every surface of our world [71–74]. The "great garbage patches" —essentially

floating columns of plastic the size of the state of Texas [75–77] in every geographical ocean—are glaring reminders of the negative impact a material type most people use (and discard) every day can have on the environment. Furthermore, a layer of plastic waste is a key characteristic of what is referred to as the "Anthropocene" geological period in which humanity now resides [78]. The ease at which polymeric waste is discarded can easily be illustrated by a ball point pen; when a small amount of ink is used up, a relatively large amount of polymeric material is discarded (Fig. 1).

Fig. 2.1 The wasteful nature of society's use of plastics.

Though recycling is one option for the reduction of polymeric waste, challenges such as contamination by filler materials or mixed plastics, robustness of recycled materials (as compared to virgin material), and the amount of energy needed to sort, separate, and reprocess plastics inhibit the viability of this path [79]. It has recently been reported that only 20% of polymeric material waste is recycled and that the strategy of chemical upcycling of polymeric waste into new materials is a more viable and value-added path [80].

The research presented in this work is based on the belief that polymer waste can be reduced by the implementation of polymeric materials with shape memory and self-healing properties that would allow components fabricated from these plastics to be easily repaired rather than be thrown away. The initial inspiration for this research effort came from a personal experience by the one of the authors involving the protective case of his child's Amazon Kindle tablet. The case had become mechanically stretched out from use (Fig. 2) and the ability to sustain an impact was compromised. The initial thought was to throw the case away and purchase a new

one. However, it was found that the case was manufactured from Ethylene-Vinyl Acetate (EVA) foam, a material with shape memory properties and a recovery temperature range between 60° and 78° C [81]. The case was thermally recovered by placing the case in in a toaster oven and the case was then able to be used again. This simple example demonstrates three key aspects related to how society views polymeric materials: 1) the need to overcome what has become an instinctive response related to throwing plastic items away; 2) the need to exploit inherent properties of polymeric materials that may increase the lifespan of components and reduce the frequency of replacement; and 3) the need to proliferate knowledge related to the ability of materials to be easily healed allowing for plastic part reuse.

CASE DAMAGED FROM USE. TYPICAL RESPONSE IS TO THROW IN TRASH! | RECOVER ORIGINAL SHAPE BY THERMAL PROCESSING | "HEALED" CASE CAN BE USED AGAIN! LESS WASTE REALIZED!

Fig. 2.2. Using the inherent shape memory properties of EVA to reuse a tablet case.

Shape memory polymers have been well studied in literature, where the critical parameters used to evaluate the characteristics of a given material system are shape recovery ratio (R_r) and shape fixation ration (R_f) given by the following equations:

$$R_r(\%) = \frac{\varepsilon_m - \varepsilon_p}{\varepsilon_m} \times 100\% \qquad (1)$$

$$R_f(\%) = \frac{\varepsilon_u}{\varepsilon_m} \times 100\% \qquad (2),$$

where ε_m is the maximum strain the specimen is subjected to (usually 100% elongation), ε_u is the elongation of the specimen after the load is removed, and ε_p is the elongation of the specimen after the recovery process [1–82–88]. To add an aspect of resiliency to the evaluation of shape memory

properties, equations (1) and (2) can be rewritten to include the variable N to include the number of cycles a specimen is subjected to [89]:

$$R_r(\%) = \frac{\varepsilon_m - \varepsilon_p(N)}{\varepsilon_m} \times 100\% \qquad (3)$$

$$R_f(\%) = \frac{\varepsilon_{u(N)}}{\varepsilon_m} \times 100\% \qquad (4)$$

The characterization of self-healing of polymers can be made by calculating the self-healing efficiency, which is calculated by various methodologies, but generally involves the comparison of mechanical properties of specimens that have been cut and then healed to control specimens [90]. For example, work conducted by Xu et al. [91] involving a shape memory polymer blend system of thermoplastic urethane (TPU) and polycaprolactone (PCL) with various amounts multi-wall carbon nanotubes (MWCNTs) determined the self-healing efficiency by comparing the Young's modulus of control specimens with those that were healed after cutting and following facile equation following a methodology as described by Wool and O'Connor [92]:

$$R(E) = \frac{E_{cut}}{E_{pristine}} \times 100\% \qquad (5),$$

where R(E) is the self-healing efficiency based on Young's modulus. Following the same concept, percent elongation (%El) and ultimate tensile strength (UTS) can also be used to determine the self-healing efficiency of a polymer using the following equations:

$$R(\varepsilon) = \frac{\varepsilon_{cut}}{\varepsilon_{pristine}} \times 100\% \qquad (6)$$

$$R(\sigma) = \frac{\sigma_{cut}}{\sigma_{pristine}} \times 100\% \qquad (7)$$

where ε and σ refer to the %El at break and UTS, respectively [92–93]. Expressing in terms of a percent gives a quantifiable metric for determining the ability of a polymeric material to retain a given physical property, E, σ, ε, among others, after being subjected to a healing process. However, considering the example mentioned above related to the tablet case, damage to a polymer

41

great enough to cause a component to be discarded as waste does not necessitate total breakage, rather deformation of a polymer component can render it useless. Therefore, developing a parameter based on how well a material can be recovered from various levels of damage is essential for understanding the resilience of a polymeric material with shape memory and self-healing properties. The work presented here demonstrates the development of a self-healing parameter. Three shape memory polymer blends were explored: 1) a SMP blend composed of acrylonitrile butadiene styrene (ABS) and styrene ethylene butylene styrene with a maleic anhydride graft (SEBS-g-MA) in a 50:50 by weight ratio, whose shape memory properties were originally characterized by Chávez et al. [83]; 2) a SMP blend composed of PLA and TPU in a 50:50 by weight ratio originally characterized by Quiñones et al. [82]; and 3) a SMP blend composed of PLA and SEBS-g-MA also composed by Quiñones et al. [82]. The ability of this material to recover from different levels of damage and still retain mechanical properties. The effect of manufacturing process on self-healing capability was also explored by comparing specimens that were fabricated by the additive manufacturing (AM) process of fused filament fabrication (FFF) to those that were manufactured by injection molding (IM). Additionally, we have demonstrated the use of various forms of SEBS to be a suitable modifier of rigid polymers in the development of FFF-specific feedstock materials [94–98].

Materials and Methods

FILAMENT FABRICATION

The PLA stock material used in this study was sourced from NatureWorks, LLC (Ingeo Biopolymer Grade 4043D, NatureWorks, LLC, Minnetonka MN, USA) in the form of pellets. The specific grade, 4043D, was chosen because it is regarded to be a commercially pure form of PLA free of additives such as crystallization promoters or impact modifiers. The thermoplastic

elastomers used in this study, SEBS and TPU, were supplied by Kraton (Grade FG1901-GT, Kraton, Houston, TX, USA) and NinjaFlex (Fenner, Inc. Manheim, PA, USA) respectively. The former was acquired in the form of pellets while the latter was in the form of 1.75mm diameter filament sold for use in 3D printers. Stock material for the fourth and final polymer, ABS, was supplied by SABIC (grade MG94, SABIC, Pittsfield, MA, USA) in the form of pellets. In order to facilitate blending, the TPU in filament form was pelletized using a Collin Teachline strand pelletizer (Collin Lab and Pilot Solutions, Norcross, GA, USA). Prior to material blending and extrusion, all four materials were dried in a compressed air dryer (Dri-Air CFAM Micro-Dryer, East Windsor, CT, USA) according to each manufacturer's recommendations. Once fully dry, three different polymer blends were created using a Collin twin screw extruder (model ZK-25T): a 50/50 by weight blend of PLA and SEBS, a 50/50 by weight blend of ABS and SEBS, and a 50/50 by weight blend of PLA and TPU. Each of the blends was extruded to a target diameter of 2.85mm for use in our FFF-type 3D printers. The extrusion parameters for each blend are shown in Table 2.1 below.

TABLE 2.1 EXTRUSION PARAMETERS FOR EACH POLYMER BLEND.

Extrusion Parameters (Collin ZK-25T)			
	PLA 4043D/SEBS-g-MA	ABS MG94/SEBS-g-MA	PLA 4043D/TPU
Zone 1 (°C)	175	200	180
Zone 2 (°C)	180	215	185
Zone 3 (°C)	180	215	185
Zone 4 (°C)	180	205	185
Zone 5 (°C)	175	190	180
Zone 6 (°C)	175	190	175
Barrel Pressure (bar)	90	90	90
Barrel Screw Speed (RPM)	16*	12*	14*
Melt Pump Screw Speed (RPM)	12	12	12

*Extruder varies the barrel screw speed continuously to maintain the pressure set point of 90 bar.

SAMPLE FABRICATION

Tensile test samples were fabricated according to ASTM D638 Type IV [99] geometry using two different methods, FFF-type 3D printing and traditional injection molding. Samples were additively manufactured with a Lulzbot Taz 5 3D printer (Fargo Additive Manufacturing Equipment 3D, LLC, Fargo, ND, USA) and injection molded with an LNS Technologies manual injection molder and a custom machined ASTM D638 Type IV aluminum mold. (Model 150A, LNS Technologies, Scotts Valley, CA, USA). Samples for analysis via DMA were additively manufactured according to the ASTM D4065 [100] standard. Both the additively manufactured tensile specimens and the DMA specimens were fabricated with a longitudinal raster pattern where the print rasters were parallel with the length of the specimen (Fig. XXX). All additively manufactured tensile samples and DMA specimens were printed with 100% infill. We chose the longitudinal raster pattern in particular for the tensile specimens because the direction of applied force during the tensile test acts parallel to the raster direction and we have found this raster pattern to provide optimal results as compared to other print raster schemes [82–83–101]. The printing parameters for each material blend are shown in Table 2.2. The temperatures at which each material was injection molded and at which the aluminum mold was pre-heated are shown in Table 2.3.

TABLE 2.2 PRINTING PARAMETERS FOR EACH POLYMER BLEND.

Printing Parameters (Lulzbot Taz 5)			
	PLA 4043D/SEBS-g-MA	ABS MG94/SEBS-g-MA	PLA 4043D/TPU
Nozzle Temperature (°C)	230	250	250
Bed Temperature (°C)	60	90	60
Nozzle Diameter (mm)	0.5	0.5	0.5
Infill Percentage (%)	100	100	100
Layer Height (mm)	0.2	0.2	0.2
Printing Speed (mm/min)	1800	1800	1800

TABLE 2.3 INJECTION MOLDING PARAMETERS FOR EACH POLYMER BLEND.

Injection Molding Parameters (LNS Injection Molder)			
	PLA 4043D/SEBS-g-MA	ABS MG94/SEBS-g-MA	PLA 4043D/TPU
Injection Temperature (℃)	200	210	200
Mold Temperature (℃)	25	55	25
Preheat Time (mins)	5	5	5

MECHANICAL TESTING

DMA data was acquired via a PerkinElmer DMA 8000 (PerkinElmer, Waltham, MA, USA) using a dual cantilever setup following ASTM D4065 operating parameters and a temperature sweep appropriate for each material blend. The temperature range selected for testing needed to encompass the glass transition temperatures of both polymers in each given blend, one of which was well below 0℃. This low temperature was achieved using a liquid nitrogen dewar connected to the testing apparatus and controlled by the DMA software. This DMA data was used to determine the temperature used for the shape memory recovery process. The DMA test parameters are shown in Table 2.4.

TABLE 2.4 DMA TESTING PARAMETERS FOR EACH POLYMER BLEND.

DMA Testing Parameters (PerkinElmer DMA 8000)			
	PLA 4043D/SEBS-g-MA	ABS MG94/SEBS-g-MA	PLA 4043D/TPU
Initial Temp (℃)	-40	-80	-80
Final Temp (℃)	110	150	100
Heating Rate (℃/min)	2	2	2
Frequency (Hz)	1	1	1

Tensile data for each material system was collected according to the ASTM D638 standard using an MTS Tensile Testing Machine with a 10KN load cell and mechanical extensometer.

Baseline tensile data was collected for each of the three material blends in both additively manufactured and injection molded forms. In order to evaluate the effect of the shape memory recovery process on the tensile strength of each polymer blend, three batches of samples were deformed to predetermined percentages of their gauge lengths (25%, 50%, and 100%) and then pulled to failure after they had been recovered at elevated temperature. The results of these tensile tests were compiled and a trendline created to fit the change in tensile strength as a function of the amount of deformation from which the samples were recovered.

SHAPE MEMORY CHARACTERIZATION

Shape memory properties were evaluated using methods previously established by previous works conducted by our group [82–83–102]. The three batches of five samples were pulled in the tensile tester to different amounts of elongation: one batch was pulled to 100% of the specified 25mm gauge length, the second batch was pulled to 50% of the gauge length, and the final batch was pulled to 25% of the gauge length. Two separate studies were performed to elucidate the effect of dwell time at maximum strain: 1) a group of samples that were promptly removed from the tensile tester once the intended amount of elongation was reached; and 2) a group of samples that was allowed to dwell at maximum strain for 5 minutes. For the two different groups of dwell time samples, three batches of 5 samples were recovered together in a horizontal air flow oven (Model 3.65, VWR International, Radnor, PA, USA) at temperatures determined according to the results of the DMA testing for each material blend. After recovery, the samples were then pulled to failure in the tensile tester. Length measurements were taken before deformation, after deformation, and after recovery for shape memory property calculation purposes using a precision digital caliper.

Shape memory properties were analyzed by calculating the shape fixation ratio (R_f) (Equation 1) and shape recovery ratio (R_r) (Equation 2) were using the following equations established in literature [88]

$$R_f(\%) = \frac{\varepsilon_u}{\varepsilon_m} \times 100 \qquad (1)$$

$$R_r(\%) = \frac{\varepsilon_m - \varepsilon_p}{\varepsilon_m} \times 100 \qquad (2)$$

$$SMI(\%) = (R_r \times R_f) \times 100 \qquad (3)$$

where ε_m is the maximum strain to which the samples were subjected, ε_u is the strain of the specimen after the load was removed, and ε_p is the final strain after being recovered at the designated recovery temperature for the polymer blend. Shape memory index (Equation 3) was calculated to help deconvolute the difference between a rubbery material – which will recover its original shape well without holding a temporary shape well – and a shape memory material which will ideally hold a temporary shape well along with recovering its original shape accurately.

SEM IMAGING

After mechanical testing, the fracture surfaces of representative samples were analyzed by scanning electron microscopy (SEM) using a Hitachi SU-3500 Variable Pressure SEM (Hitachi America, Ltd., Santa Clara, CA, USA). Due to charging of the samples, imaging was performed at a pressure of 90Pa either using a backscattered electron detector (BSE) or an ultra-variable detector (UVD) at an accelerating voltage between 10-15 kV.

X-RAY CHARACTERIZATION

A short study was performed to determine the extent of crystallization in our PLA/SEBS blend which occurs during annealing. Characterization was performed using a Bruker D8 Discover X-Ray Diffractometer (Bruker Scientific LLC, Billerica, MA, USA) equipped with a Cu

K-α (λ = 1.54 Å) source. Annealing was performed according to previous research performed by our group on PLA and PLA-based composites where crystalline peaks are observable on XRD after subjecting specimens to an annealing schedule of 120°C for 20 minutes [103–104]

Experimental Results

INITIAL CHARACTERIZATION

DMA testing was used in order to determine the temperature for the shape recovery processing. Values obtained during testing were the max tan δ temperature and the glassy onset temperature as determined by storage modulus drop off as described in the ASTM D4065 standard [105]. In previous work done by this lab glassy onset temperature was used for programming high temperature deformation schedules for shape memory samples; however, this study investigates room temperature deformation, so the only values of note were the max tan δ values. The DMA curves for PLA/SEBS, ABS/SEBS, and PLA/TPU are shown in Figures 2.1, 2.2, and 2.3 respectively. As shown in previous studies, exposing the sample to a temperature above that of the max tan δ will induce the shape recovery phenomenon. The results gathered from the DMA testing show a max tan δ value of 0.710 at 63.08°C for the PLA/SEBS blend, a max tan δ value of 0.810 at 116.23°C for the ABS/SEBS blend, and a max tan δ value of 0.756 at 63.88°C for the PLA/TPU blend. As seen in Figure 2.3, there are two peaks in the tan delta curve for the PLA/SEBS blend which likely indicates that the two polymers did not mix well. Previous work has shown that PLA and SEBS do not mix well using scanning transmission electron microscopy (STEM) imaging to see that there are two distinct phases present in the blend [82]. Recovery temperature of 70°C was selected for both the PLA/SEBS and PLA/TPU blends while a recovery temperature of 120°C was selected for the ABS/SEBS system.
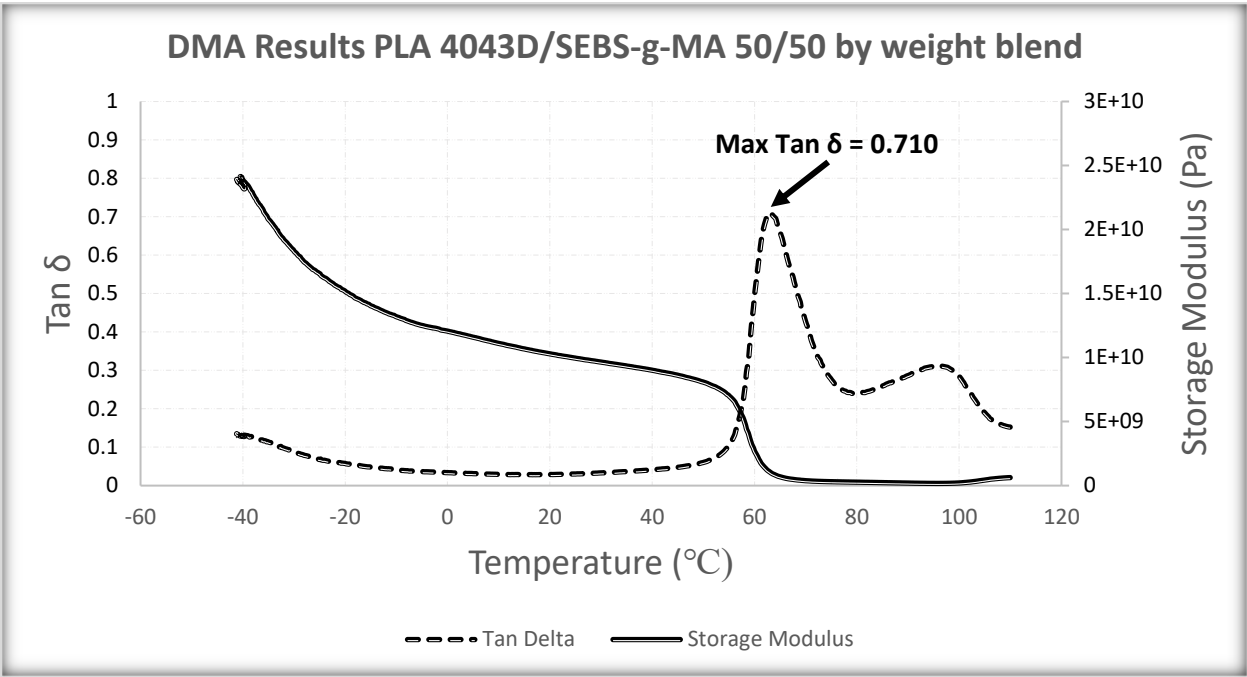
Figure 2.3 DMA results for the blend of PLA 4043D and SEBS-g-MA.
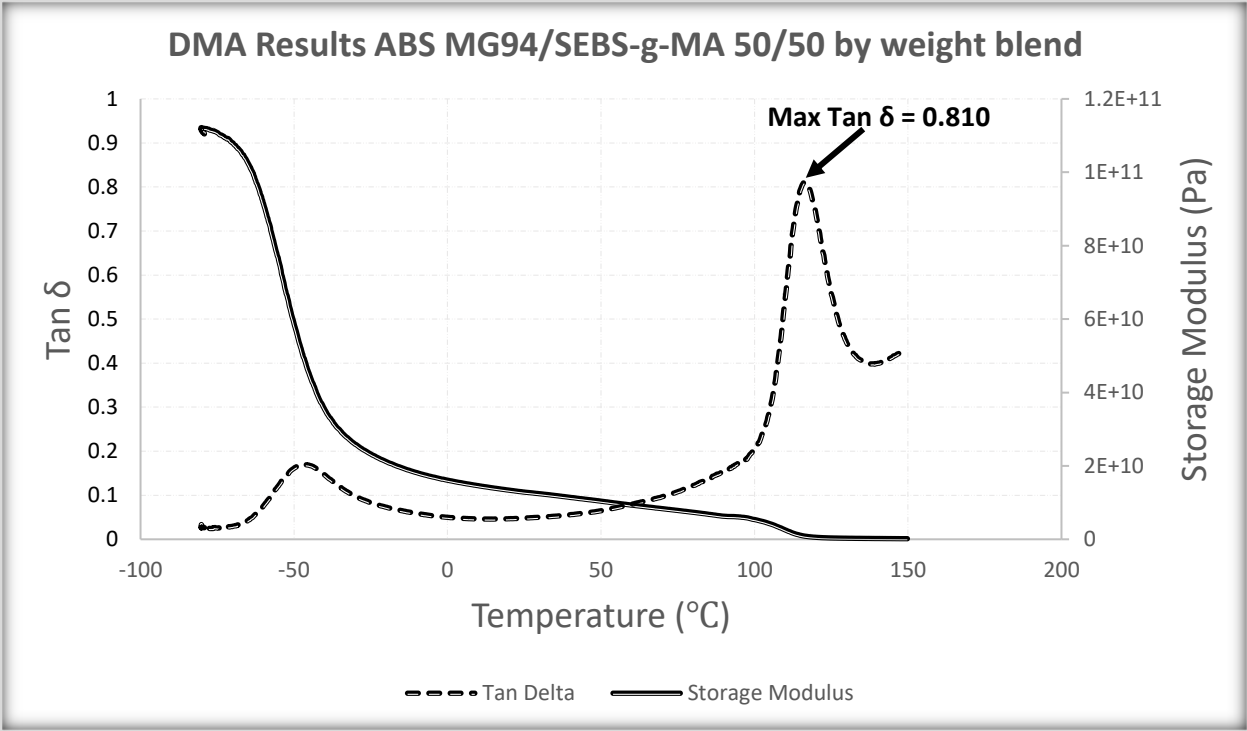
Figure 2.4 DMA results for the blend of ABS MG94 and SEBS-g-MA.
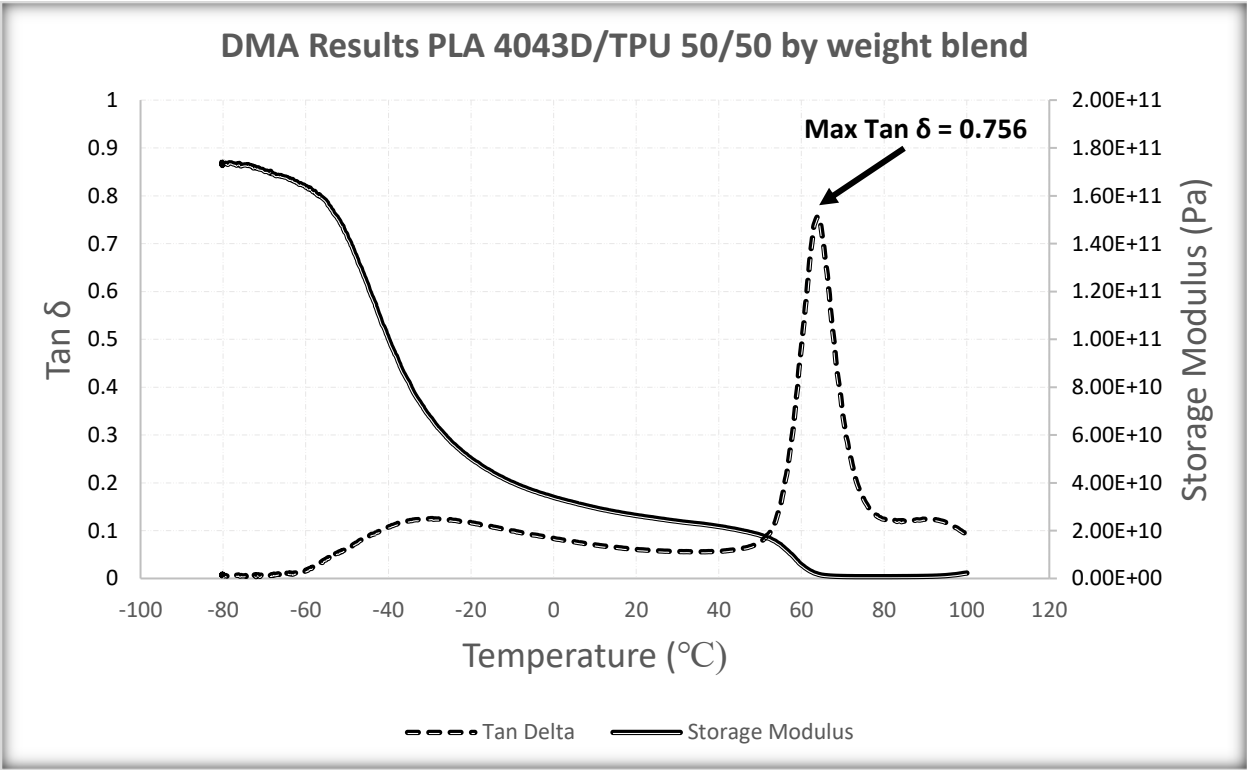
Figure 2.5 DMA results for the blend of PLA 4043D and Ninjaflex TPU.

X-Ray Characterization

Results of the x-ray characterization for the PLA/SEBS blend is shown in Figures XXX and the results for the ABS/SEBS blend are shown in Figures XXX. It is shown that no crystallinity was induced via either the strain or the temperature that the samples were subjected to. The spectra look identical in each of the as-printed, elongated, and recovered conditions for both polymer blends. The only crystallization appears in PLA when it has been annealed for 5 minutes at 120°C [103–104]. The results of this test confirm that the materials are not becoming semi-crystalline during the deformation and recovery processes.

a)

b)

c)
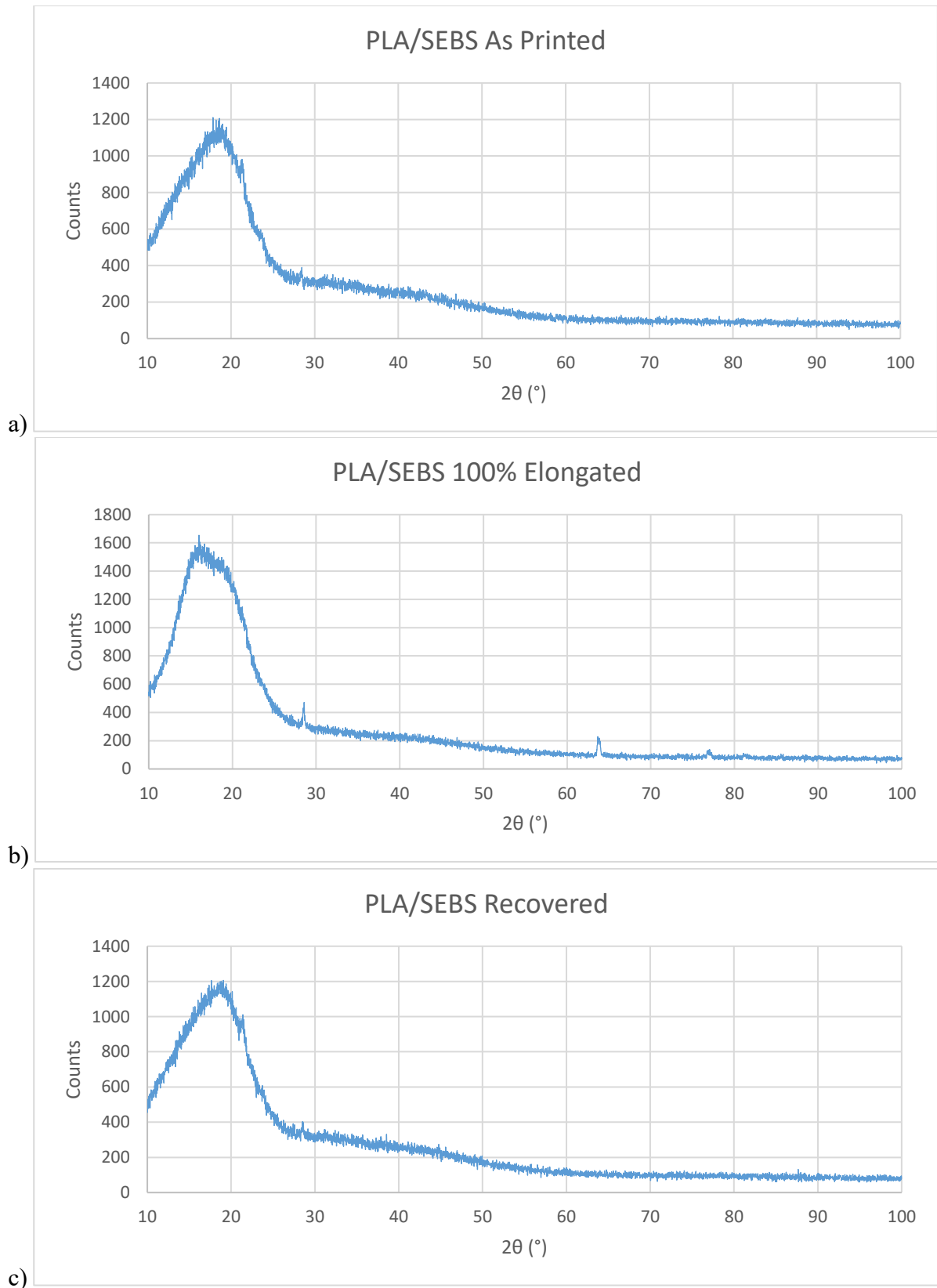
Figure 2.6 XRD spectra of the PLA/SEBS blend in a) as-printed, b) elongated, and c) recovered forms.

52
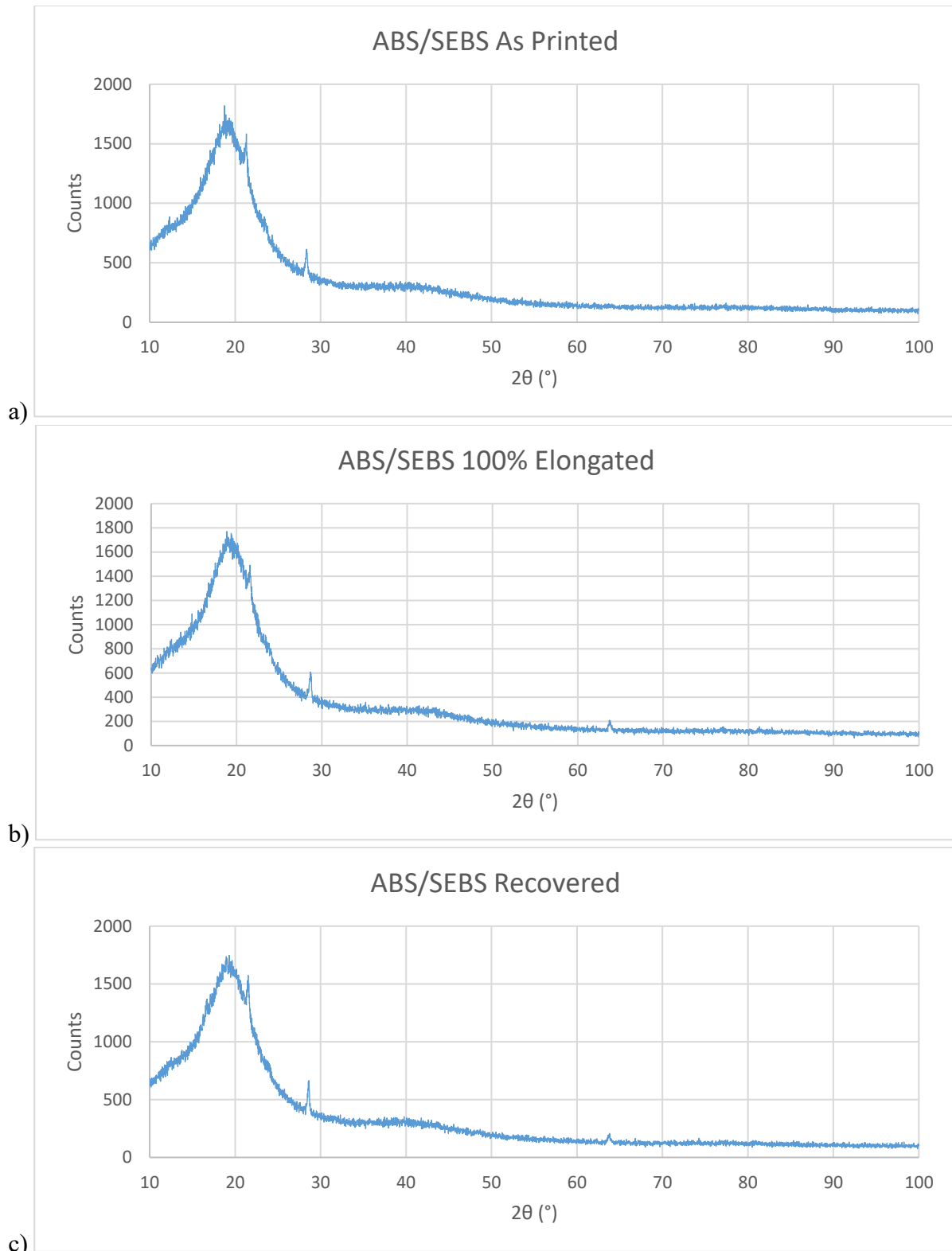
Figure 2.7 XRD spectra of the ABS/SEBS blend in a) as-printed, b) elongated, and c) recovered forms.

MECHANICAL TESTING

PLA 4043D/SEBS-g-MA

Additively Manufactured: The blend of PLA 4043D and SEBS-g-MA showed the highest average tensile strength in the as printed form with an average of 25.26 ± 0.27 MPa. It is shown that the average tensile strength decreased with increasing amount of deformation from which the sample was recovered. After recovering from 25%, 50%, and 100% elongation the average tensile strength dropped to 24.68 ± 1.19, 23.38 ± 2.31, and 21.98 ± 0.61 MPa respectively for the samples with no dwell time. The samples allowed to dwell showed exceptionally similar results with the average tensile strength decreasing from 23.43 ± 1.27, to 24.26 ± 4.61, to 21.1 ± 0.54 MPa for 25%, 50%, and 100% elongation recovery respectively. Allowing the samples to dwell under load at their prescribed amount of deformation did not make a significant difference in the tensile strength exhibited.

Injection Molded: Just like the results of the additively manufactured samples, the injection molded samples showed their highest average tensile strength in the as fabricated form with consistently decreasing values as the amount of deformation from which they were recovered increased. The tensile strength was nearly identical to the additively manufactured samples, only differing by ~1 MPa at the most with the highest value occurring for the as-fabricated samples with dwell time at an average of 26.4 ± 1.4 MPa. The rate of decrease in tensile strength with increase in deformation amount also mirrored those shown in the 3D printed samples with the tensile strength dropping from 24.6 ± 0.95, to 25.9 ± 0.33, to 22.67 ± 2.46 MPa for 25%, 50%, and 100% elongation respectively. Dwell time did not make a significant difference in the amount of tensile strength which was lost for the varying amounts of deformation. The batch of samples which were not allowed to dwell showed an overall lower tensile strength compared to the ones

allowed to dwell. This difference is likely due to the fact that the batches were fabricated several months apart rather than because of the dwell time. The results of the tensile testing for this blend are shown in Figure 2.4.
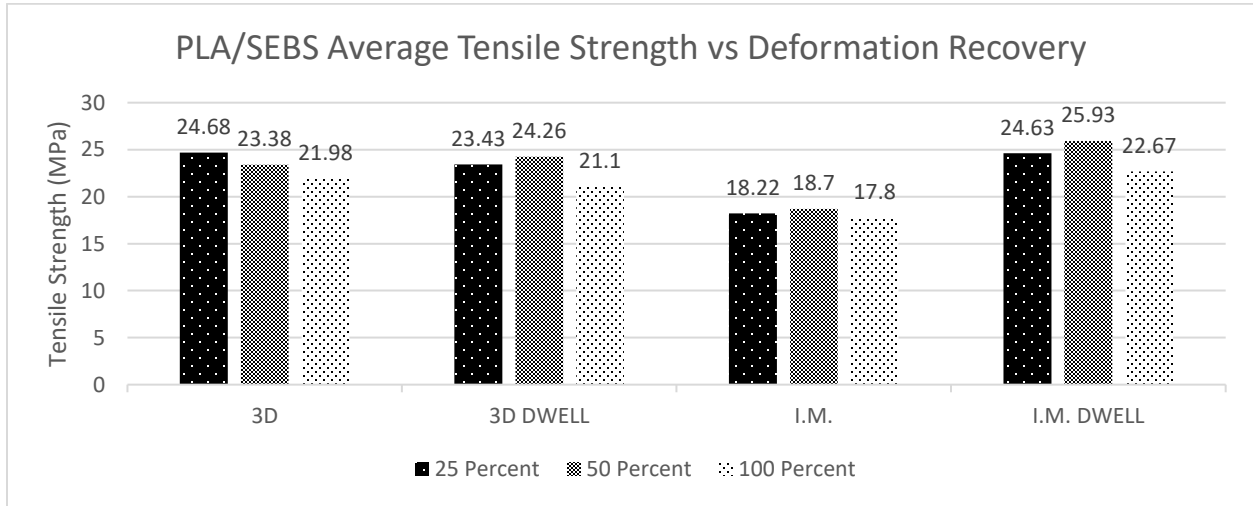
Figure 2.6 Comparison of average tensile strength for all test batches of the PLA/SEBS blend.

ABS MG94/SEBS-g-MA

Additively Manufactured: This polymer blend showed very consistent tensile strength in its 3D printed form regardless of the amount of deformation from which the samples were recovered. The tensile strength was 20.42 ± 0.41, 20.56 ± 0.22, and 20.3 ± 1.48 MPa for the 25%, 50%, and 100% deformation batches respectively when the samples were not allowed any dwell time. Considering a baseline tensile strength of 20.32 ± 0.62 MPa, the blend shows an impressive ability to maintain its strength even after deformation and recovery. Interestingly, adding a five-minute dwell time under load at the prescribed amount of deformation led to a very small increase in strength as the amount of deformation increased. The average tensile strength for the samples in this group were 19.23 ± 0.26, 19.43 ± 0.12, and 20 ± 0.59 MPa for the 25%, 50% and 100% deformation groups respectively. Though the strength is increasing along with the amount of

deformation recovery, the samples never quite reach their baseline tensile strength indicating that the addition of the dwell time may very slightly weaken the samples.

Injection Molded: The injection molded batches of samples, both with and without dwell time in the test schedule, showed a very consistent average tensile strength as the amount of deformation from which they were recovered increased. The average tensile strength for the samples without dwell time was just slightly lower than that of the baseline tensile strength exhibited by the as-fabricated samples: 22.32 ± 0.07 MPa. The batch of samples that were not allowed to dwell showed an average tensile strength of 21.82 ± 0.07, 21.7 ± 0.24, and 21.74 ± 0.40 MPa for the 25%, 50%, and 100% deformation groups respectively. The batch of samples which were allowed to dwell for five minutes at load showed an average tensile slightly lower than that of both the baseline and no-dwell samples. The average tensile strength was 21.56 ± 0.40, 21.3 ± 0.08, and 20.73 ± 1.51 MPa for the 25%, 50%, and 100% deformation groups respectively. This shows a very slight downward trend for the tensile strength as the amount of deformation increased. This batch of samples was the only one for this blend of polymers which showed this trend in a significant way. Shown below in Figure 2.5 are the results of the tensile testing for this polymer blend.
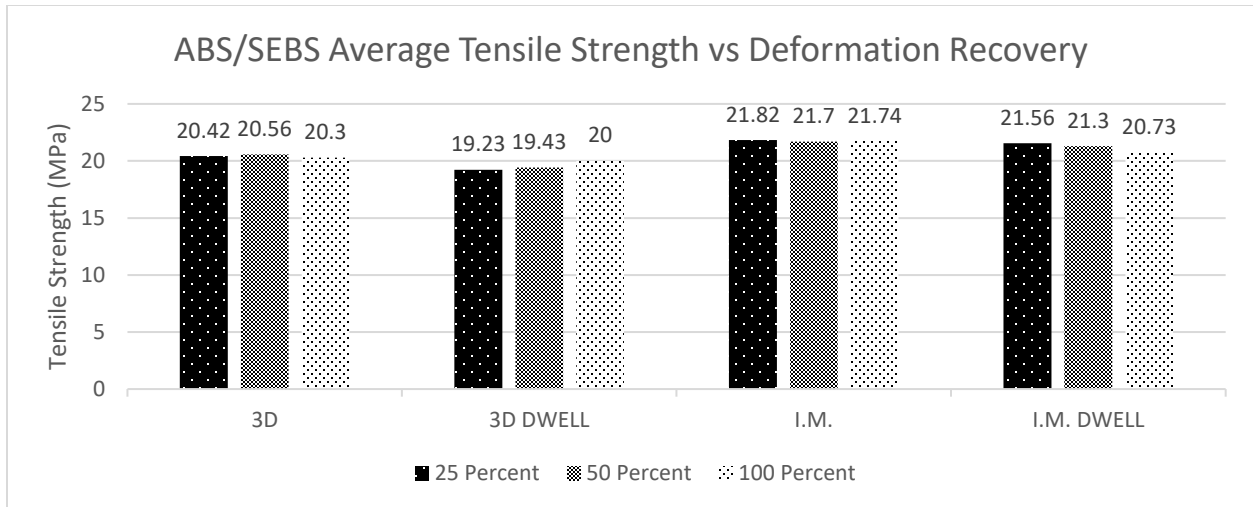
Figure 2.7 Comparison of average tensile strength for all test batches of the ABS/SEBS blend.

PLA 4043D/TPU

Additively Manufactured: This blend of polymers was the most inconsistent in mechanical properties, especially between the two fabrication methods. The average tensile strength for this blend in the as-printed form was 30.42 ± 1.03 MPa. Subjecting the samples to the deformation and recovery process led to a very significant decrease in average tensile strength. In the case of the 3D printed batches of samples, the ones which were allowed to dwell under load showed a much higher average tensile strength compared to the ones which were not given a dwell time. Also, the batch of samples allowed to dwell showed the opposite trend of tensile strength change with amount of deformation as compared to the batch of samples with no dwell. As shown in Figure 9, it is very obvious that the strength decreased when not allowed to dwell and increased when allowed to dwell. The no-dwell samples showed an average tensile strength of 19.52 ± 1.38, 13.64 ± 3.96, and 12.12 ± 5.15 MPa for the 25%, 50%, and 100% deformation groups respectively while the samples allowed to dwell showed an average tensile strength of 24.36 ± 0.90, 25.96 ± 2.46, and 26.9 ± 5.33 MPa for the 25%, 50%, and 100% deformation groups respectively. This

57

shows a dramatic increase in overall tensile strength with the addition of dwell time to the test schedule.

Injection Molded: Injection molding this blend of polymers gave very inconsistent results. The first batch of blended material was used to create the samples which would not be allowed to dwell under load. Unilaterally, these samples ruptured well before reaching their prescribed amount of deformation. The second batch of material was blended and fabricated into test samples with the exact same batches of material 4 months after the first was done. However, this batch of samples was able to reach their prescribed amount of deformation without issue and showed greatly increased average tensile strength along with a trend of increasing strength with increasing amount of deformation recovery as compared to the 3D printed counterparts. The injection molded samples allowed to dwell showed an average tensile strength of 36.16 ± 0.87, 40.63 ± 1.96, and 44.26 ± 2.03 MPa for the 25%, 50%, and 100% deformation groups, respectively. The baseline tensile strength for this polymer blend in the as-fabricated condition was 32.42 ± 1.32 MPa which is less than any of the samples which were subjected to the shape memory recovery test.

A bar graph comparing the average tensile strength of this polymer blend in both fabrication methods at all amounts of deformation is shown in Figure 2.6.
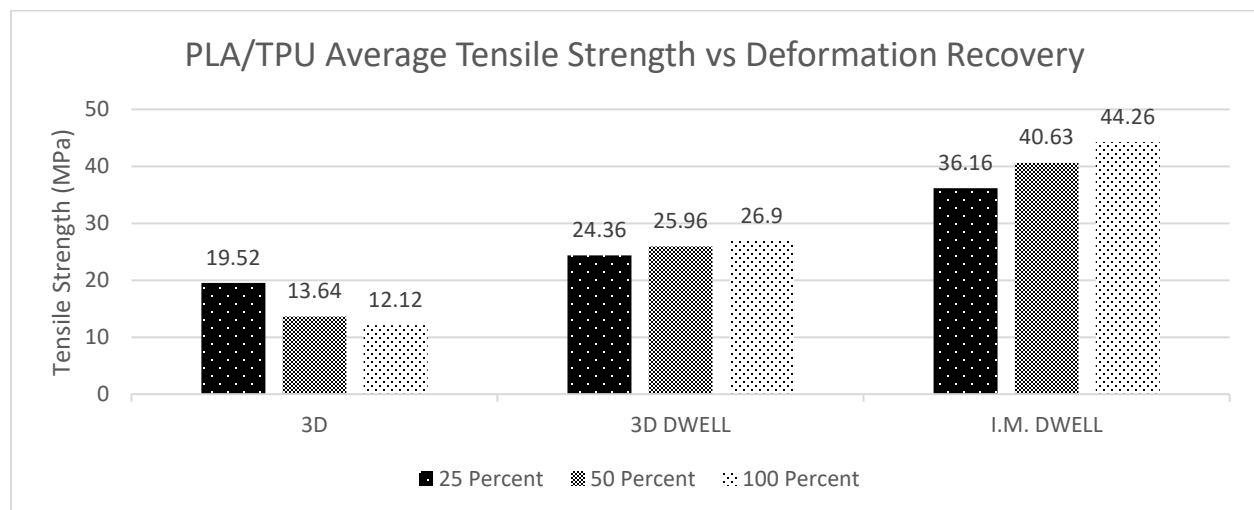
Figure 2.8 Comparison of average tensile strength for all batches of the PLA/TPU blend.

Comparison of Blends and "Self-Healing Parameter"

In this study, four different polymers were combined in three different blends and fabricated into test specimens via two different methods. Each polymer blend performed uniquely in terms of mechanical properties and shape memory properties. The best performer in terms of raw tensile strength, regardless of whether the samples were deformed and recovered, was the PLA/TPU blend in the injection molded form after recovering from 100% deformation with a five-minute dwell time under load. Right behind that combination of polymers, fabrication method, and dwell time are all of the PLA/SEBS blends except the no-dwell injection molded samples as well as the 3D printed PLA/TPU blend with dwell time. The ABS/SEBS polymer blend had the lowest average tensile strength across all batches but was also the most consistent with the lowest value being 19.23 ± 0.26 MPa and the highest being 21.82 ± 0.07 MPa. This blend showed the least sensitivity to recovery from deformation of all the blends by far.

Possibly the most significant result from this study is the development of a measurable mechanical property we are calling the "self-healing parameter." This parameter is calculated by averaging the tensile strength of each group of samples and plotting those values as points on a graph with the y-axis being tensile strength and the x-axis being the percent elongation from which the group of samples was recovered. Next, plotting a line of best fit to those points gives a linear equation describing the change in strength vs percent deformation recovered. The slope of this line being negative indicates a reduction in average tensile strength as the samples are exposed to, and recovered from, greater amounts of deformation. The slope being positive indicates the opposite: an increase in strength as the deformation amount increases. Provided that the line of

best fit matches the data set well by having an R^2 value close to 1 or 0, the y-intercept of the line will be nearly the same as the baseline tensile strength.

In order to create a unitless value for this parameter, we divide the slope of the line, *m*, by the y-intercept, *b*, while assuming the value of *x* to be equal to 1. The result is a value which indicates the percent of baseline tensile strength which is lost when deformed to 100% of the gauge length and recovered for 5 minutes at the established recovery temperature. This value was calculated for each of the polymer blends for both manufacturing methods both with and without dwell time, the results of which are shown in table 2.5.

TABLE 2.5 COMPARISON OF HEALING PARAMETERS FOR EACH TEST BATCH.

		Line of Best Fit	R^2 Value	Healing Parameter (m/y)
PLA/SEBS	3D	y = -3.3897x + 25.308	0.983	-13.39
	3D Dwell	y = -3.7657x + 25.16	0.8216	-14.97
	I.M.	y = -2.1051x + 19.696	0.6311	-10.69
	I.M. Dwell	y = -3.2834x + 26.344	0.7055	-12.46
ABS/SEBS	3D	y = -0.0274x + 20.412	0.0097	-0.13
	3D Dwell	y = -0.0571x + 19.77	0.0023	-0.29
	I.M.	y = -2.1051x + 19.696	0.6311	-10.69
	I.M. Dwell	y = -1.4949x + 22.134	0.9339	-6.75
PLA/TPU	3D	y = -17.003x + 26.364	0.7648	-64.49
	3D Dwell	y = -2.0526x + 27.808	0.1168	-7.38
	I.M.	-	-	-
	I.M. Dwell	y = 11.841x + 33.192	0.9566	35.67

This healing parameter value can be interpreted as a larger number being more favorable. If the healing parameter is negative then the material loses strength as deformation recovery is increased and the magnitude of that value indicates the rate at which strength is lost. If the healing parameter is zero then the tensile strength of the material is unaffected by the deformation and recovery process. If the healing parameter is positive then the tensile strength of the material increases as the amount of deformation recovered increases. For the purposes of evaluating the ability of a material to maintain its strength after deformation and recovery, a higher number

indicates better performance than a lower number. By comparing these values, a trend appears for each blend. The PLA/SEBS blend performs better on average when the sample is allowed to dwell, regardless of the manufacturing methods. However, both manufacturing methods showed a negative healing parameter in all cases with only minor variation in magnitude with the highest being -10.69 in the injection molded form without dwell time and the highest being -14.97 in the 3D printed form with dwell time. The ABS/SEBS showed an interesting contrast in performance between manufacturing methods. The 3D printed sample groups have nearly the same healing parameter of barely below 0 whether or not they were allowed to dwell. While the 3D printed samples showed no loss of strength after deformation and recovery, the injection molded samples showed a consistent decrease in strength with the no-dwell samples faring slightly worse than the dwell samples with values of -10.69 and -6.75 respectively. The PLA/TPU blend was the only sample group with a positive healing parameter value as well as the greatest range of healing parameters between sample groups. The 3D printed sample groups varied greatly between the dwell and no-dwell samples with values of -7.38 and -64.49 respectively. These values show a major sensitivity to dwell time in terms of retained tensile strength after deformation recovery for the 3D printed samples. The one batch of injection molded samples show the only positive healing parameter for this study with a high value of 35.67. This is the only sample group to show an increase in strength with increasing amount of deformation from which the samples were recovered.
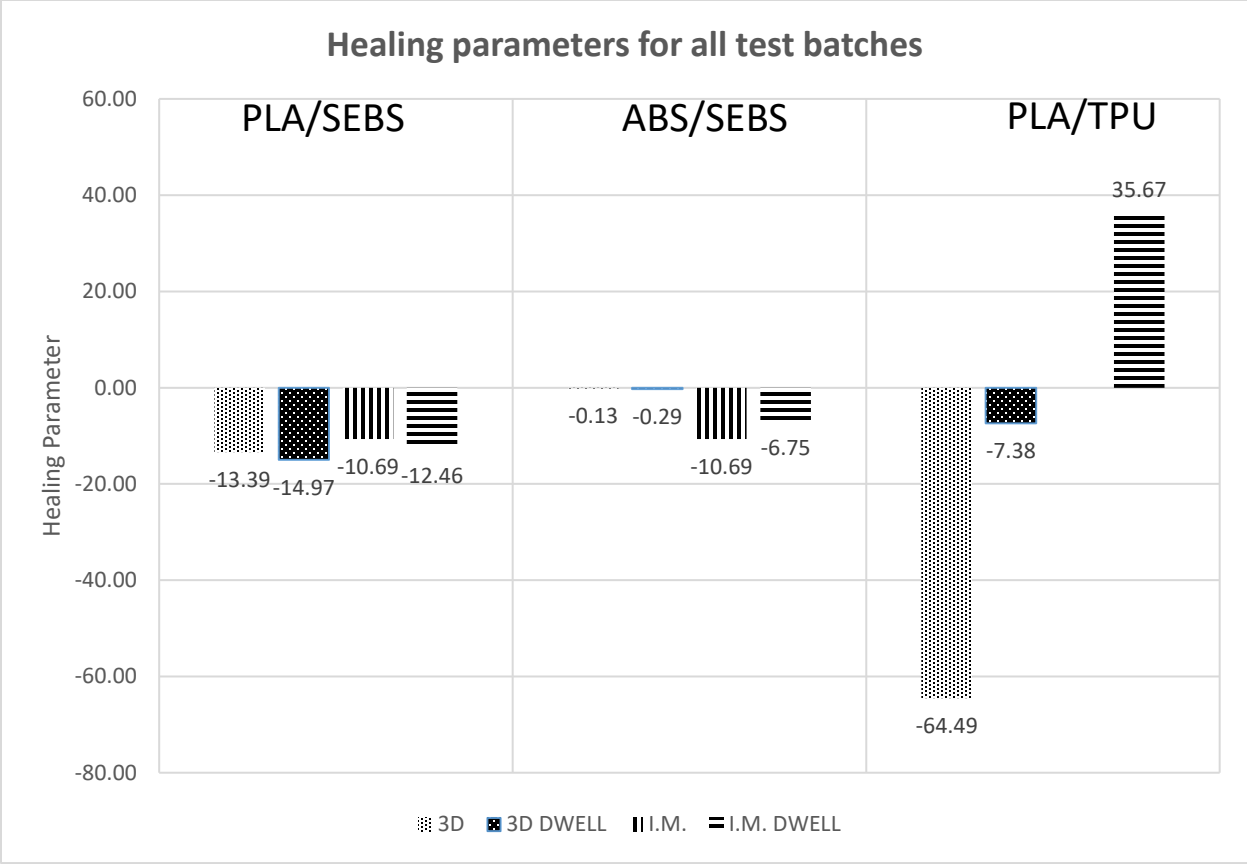
Figure 2.9 Comparison of the healing parameters for all test batches

Figure 2.9 shows a bar graph with the healing parameter for each test batch which allows the performance trends to be seen very easily. It is easily seen that the PLA/SEBS test batches were the most consistent in performance with dwell time being the most important variable. The blend of ABS/SEBS shows an easily observable pattern in which the injection molded samples performed worse than the 3D printed samples. Lastly the PLA/TPU blend deserves more investigation into its performance seeing as it has the largest range of healing parameters.

SHAPE MEMORY CHARACTERIZATION

The calculated results of the shape memory characterization study are shown for each blend in tables 2.6, 2.7, and 2.8.

PLA 4043D/SEBS-g-MA

The blend composed of PLA and SEBS-g-MA in a 50/50 by weight ratio exhibited the highest fixation ratio of all the blends with the highest being in the 3D printed form and subjected to a dwell time of 5 minutes at the prescribed amount of strain. For the 3D printed samples, the addition of the 5-minute dwell time led to a significant increase in fixation ratio which decreased in magnitude with an increase in deformation amount. The recovery ratio of this blend in 3D printed form showed a negligible change across both fabrication methods whether or not the samples were allowed to dwell. The vast majority of the samples had a recovery ratio slightly over 100% indicating a small amount of over-recovery, or shrinkage, occurring during the recovery process. Because the shape memory index is calculated using the fixation and recovery ratios, the addition of dwell time caused all the samples to show an increase directly proportional to that of the fixation ratio.

TABLE 2.6 SHAPE MEMORY PROPERTY CALCULATION RESULTS FOR ALL BATCHES OF THE PLA/SEBS BLEND.

| | PLA/SEBS Shape Memory Properties | | | | | | | | |
| | 25 Percent | | | 50 Percent | | | 100 Percent | | |
	Fixation Ratio	Recovery Ratio	Shape Memory Index	Fixation Ratio	Recovery Ratio	Shape Memory Index	Fixation Ratio	Recovery Ratio	Shape Memory Index
3D	81.66	100.95	82.44	83.50	100.43	83.86	87.34	100.24	87.55
3D DWELL	88.91	101.23	90.00	88.37	100.57	88.87	90.08	100.29	90.29
I.M.	60.58	100.36	60.80	69.41	100.10	69.48	74.26	99.96	74.23
I.M. DWELL	81.71	100.39	82.03	85.57	100.10	85.66	86.56	99.99	86.66

a)

PLA/SEBS Fixation Ratio (R_f) vs Deformation

b)

PLA/SEBS Recovery Ratio (R_r) vs. Deformation
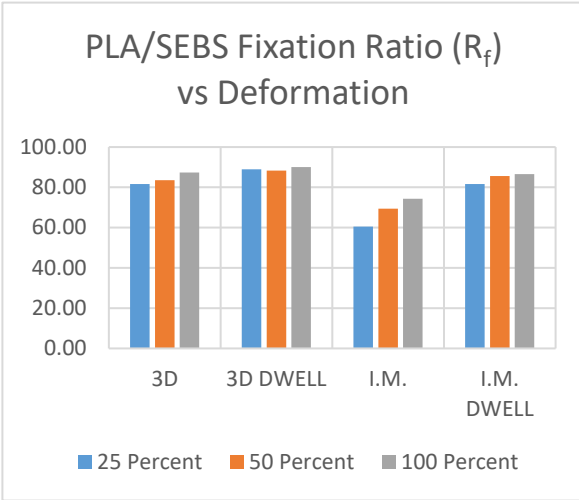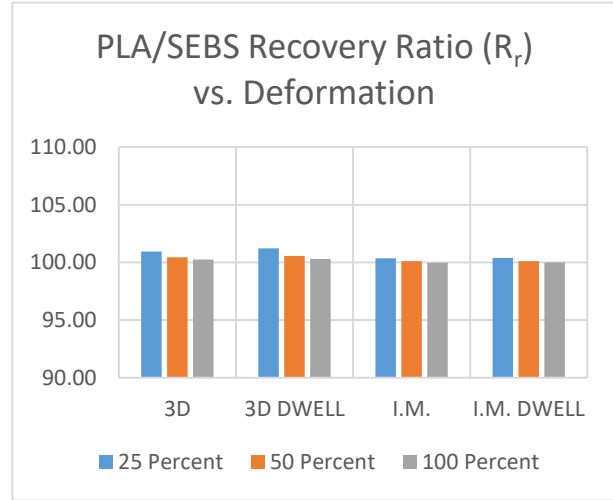
Figure 2.10 Comparison of a) fixation ratio vs deformation recovery and b) recovery ratio vs deformation recovery for all batches of the PLA/SEBS blend.

PLA/SEBS Shape Memory Index (SMI) vs Deformation
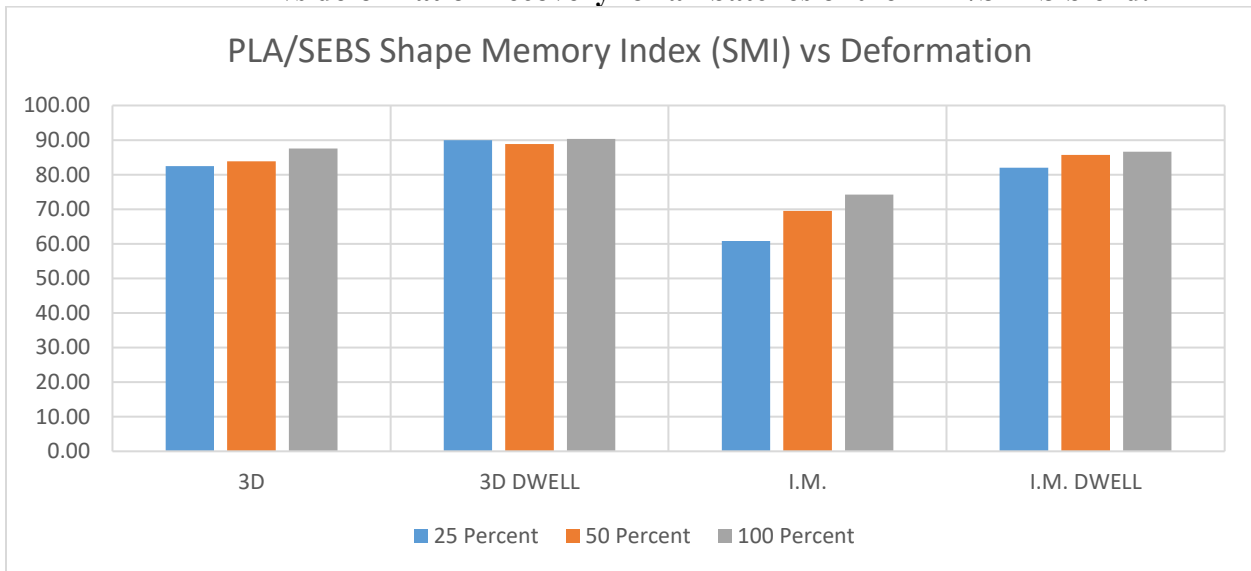
Figure 2.11 Comparison of shape memory index (SMI) vs deformation recovery for all batches of the PLA/SEBS blend.

The worst performing batch of samples for this material blend was the injection molded samples which were not allowed to dwell during the deformation process. Allowing the samples to dwell for 5 minutes produced results almost identical to that of the 3D printed samples not

64

subjected to dwell time. The recovery ratio was just over 100% for all the samples except the ones deformed to 100% of their gauge length; these were just under 100% and showed nearly perfect dimensional recovery. Due to the exceptionally poor fixation ratio, the shape memory index was also very low for the injection molded samples without dwell time. The best performing batch of samples in the context of these shape memory properties was the 3D printed with dwell time batch.

<u>ABS MG94/SEBS-g-MA</u>

Beginning with the 3D printed samples, there is a noticeable and significant improvement in the fixation ratio for the samples that were allowed to dwell under load at their maximum prescribed strain of 25% for 5 minutes. The fixation ratio was nearly identical for the samples which were stretched to 50% of their gauge length and, contrary to the 25% samples, the fixation ratio decreased very slightly when dwell time was added for the samples which were stretched to 100% of their gauge length. There was no difference in the recovery ratio between the sample batches regardless of dwell time or deformation amount and all the samples had the tendency to over-recover and end up with a final length just slightly shorter than they were as printed. The shape memory index increased significantly for the 25% samples and very slightly decreased for the 50% and 100% samples.

Table 2.7 Shape memory property calculation results for all batches of the ABS/SEBS blend.

	ABS/SEBS Shape Memory Properties								
	25 Percent			50 Percent			100 Percent		
	Fixation Ratio	Recovery Ratio	Shape Memory Index	Fixation Ratio	Recovery Ratio	Shape Memory Index	Fixation Ratio	Recovery Ratio	Shape Memory Index
3D	40.03	101.84	40.77	48.99	100.84	49.41	58.02	100.39	58.25
3D DWELL	45.07	101.43	45.71	48.27	100.70	48.60	56.18	100.27	57.11
I.M.	37.95	101.76	38.62	48.62	100.79	49.01	60.71	100.25	60.86
I.M. DWELL	49.12	101.97	50.09	56.03	101.01	56.60	65.42	100.45	65.80
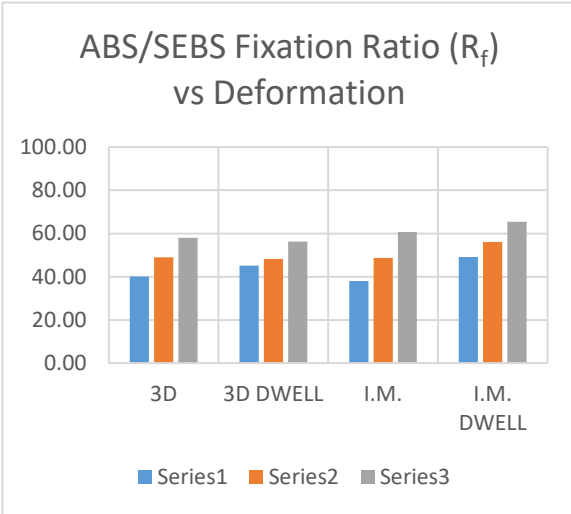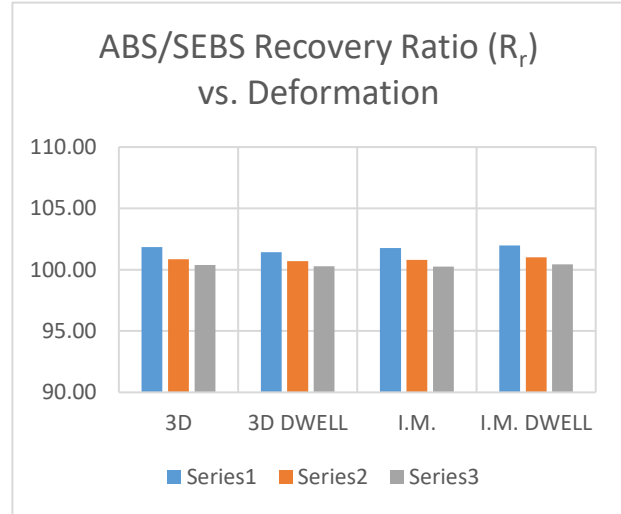
Figure 2.12 Comparison of a) fixation ratio vs deformation recovery and b) recovery ratio vs deformation recovery for all batches of the ABS/SEBS blend.
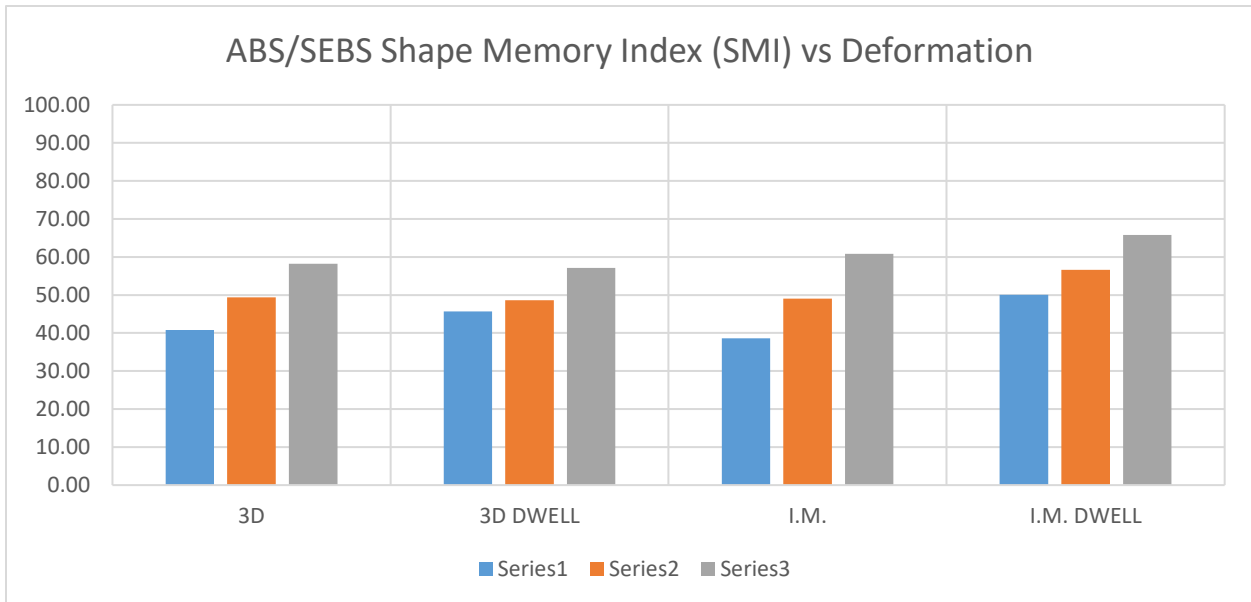
Figure 2.13 Comparison of shape memory index (SMI) vs deformation recovery for all batches of the ABS/SEBS blend.

The injection molded samples showed a similar trend to the 3D printed samples but with more consistency. The fixation ratio of the samples increased for all batches subjected to dwell

time but at a decreasing rate with increasing deformation amount. The fixation ratio increased by 12% for the 25% samples, 8% for the 50% samples, and 5% for the 100% samples. Just like the PLA/SEBS blend, the recovery ratio for these samples stayed the same regardless of dwell time or deformation amount and the values mirror those of the 3D printed samples. These results lead to an overall increase in shape memory index directly proportional to the increase in fixation ratio for each blend.

PLA 4043D/TPU

This polymer blend, much like the PLA/SEBS blend showed a significant improvement in fixation ratio when the dwell time was added to the testing schedule for the 3D printed samples. This improvement in fixation ratio was very similar in magnitude for all three deformation amounts with an average of 6% increase. The recovery ratio was nearly identical for both batches of 3D printed samples indicating that the ability for the samples to recover their original shape was not affected by the dwell time. The shape memory index increased proportionally to the increase in fixation ratio experienced by all the 3D printed samples.

Table 2.8 Shape memory property calculation results for all batches of the PLA/TPU blend.

	PLA/TPU Shape Memory Properties								
	25 Percent			50 Percent			100 Percent		
	Fixation Ratio	Recovery Ratio	Shape Memory Index	Fixation Ratio	Recovery Ratio	Shape Memory Index	Fixation Ratio	Recovery Ratio	Shape Memory Index
3D	74.94	100.19	75.09	76.02	99.96	75.98	80.02	99.86	79.90
3D DWELL	80.91	100.30	81.15	83.73	99.99	83.73	85.36	99.91	85.93
I.M. DWELL	86.72	99.90	86.63	88.72	99.76	88.50	87.86	99.64	87.43

a)
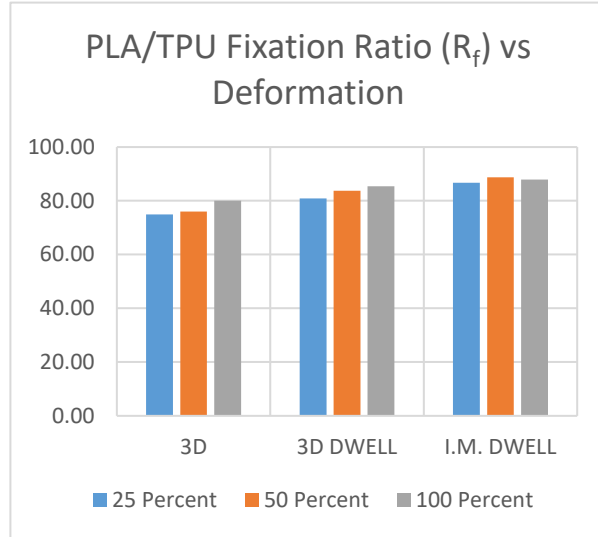
b)
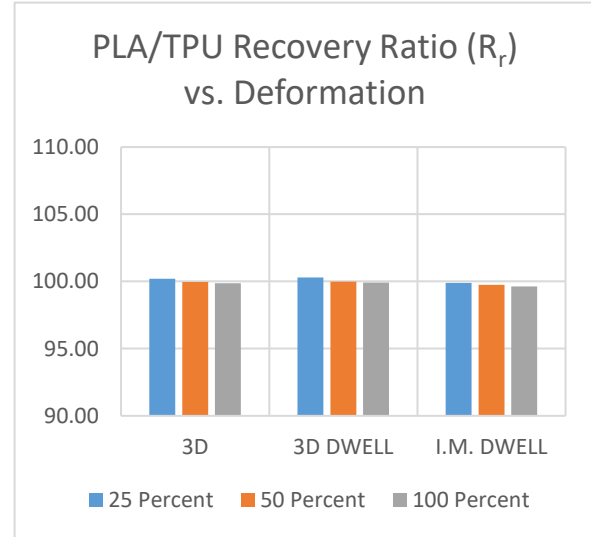
Figure 2.14 Comparison of a) fixation ratio vs deformation recovery and b) recovery ratio vs deformation recovery for all batches of the PLA/TPU blend.
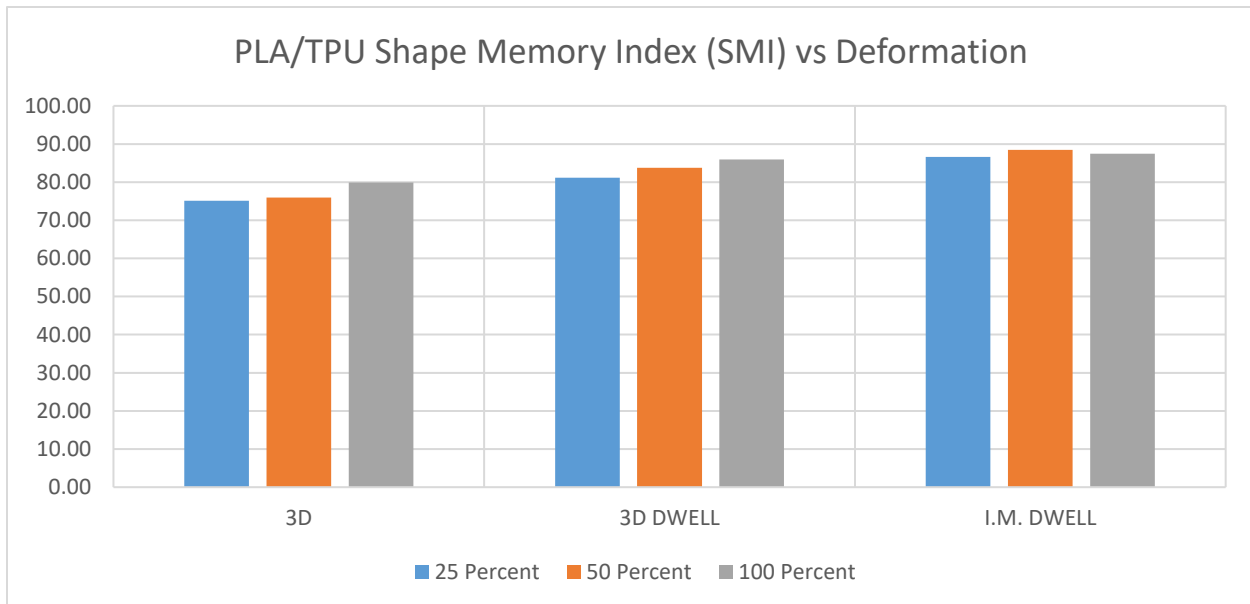
Figure 2.15 Comparison of shape memory index (SMI) vs deformation recovery for all batches of the ABS/SEBS blend.

Every sample in the first batch of injection molded samples, intended to be tested without any dwell time at load, ruptured well before reaching the prescribed amount of strain. This lack

of ductility lead to an inability to obtain shape memory data for this blend at that time. The second batch of injection molded samples, to be used for testing with a five-minute dwell time at load, showed significantly more ductility and all samples were able to achieve their prescribed amount of strain. These samples showed the best shape memory properties for this blend. The injection molded samples allowed to dwell showed an increase in fixation ratio over both 3D printed sample batches at all amounts of deformation. The recovery ratio also was the same across both fabrication methods regardless of dwell time. Just like the 3D printed samples, these showed an increase in their shape memory index proportional to fixation ratio improvement

SEM FRACTOGRAPHY

The results of the SEM fractography were mostly as expected for polymer blends composed significantly of rubbery materials with the exception being the first batch of injection molded PLA/TPU samples which all failed well before the lowest amount of prescribed strain.

Beginning with the PLA/SEBS blend manufactured via 3D printing, the fracture surfaces are very similar between the baseline (no shape memory processing) and the recovered samples. The recovered samples show a more uniform fracture surface and more easily distinguishable voids between the deposited filament on each layer. The interbead voids are very small which indicates that the print parameters are very well optimized because the individual beads have fused together well. Both un-recovered and recovered samples showed ductile fracture surface evidence which is expected with the presence of SEBS-g-MA. The injection molded samples of PLA/SEBS showed significant shrinkage in the center of the volume of the gauge section resulting in a large cylindrical void as seen in Figure 2.14. This large void is present whether or not the sample was tested as manufactured or after being subjected to the shape memory processing. For both sample batches, the fracture surface nearest to the void in the center shows much more ductile failure with

69

greater deformation as compared to the surfaces nearer to the outside surface of the sample. The contrast in fracture evidence between the inner and outer volume of the sample shows a common phenomenon of injection molding where the material nearest the mold wall cools down faster than the material in the center.
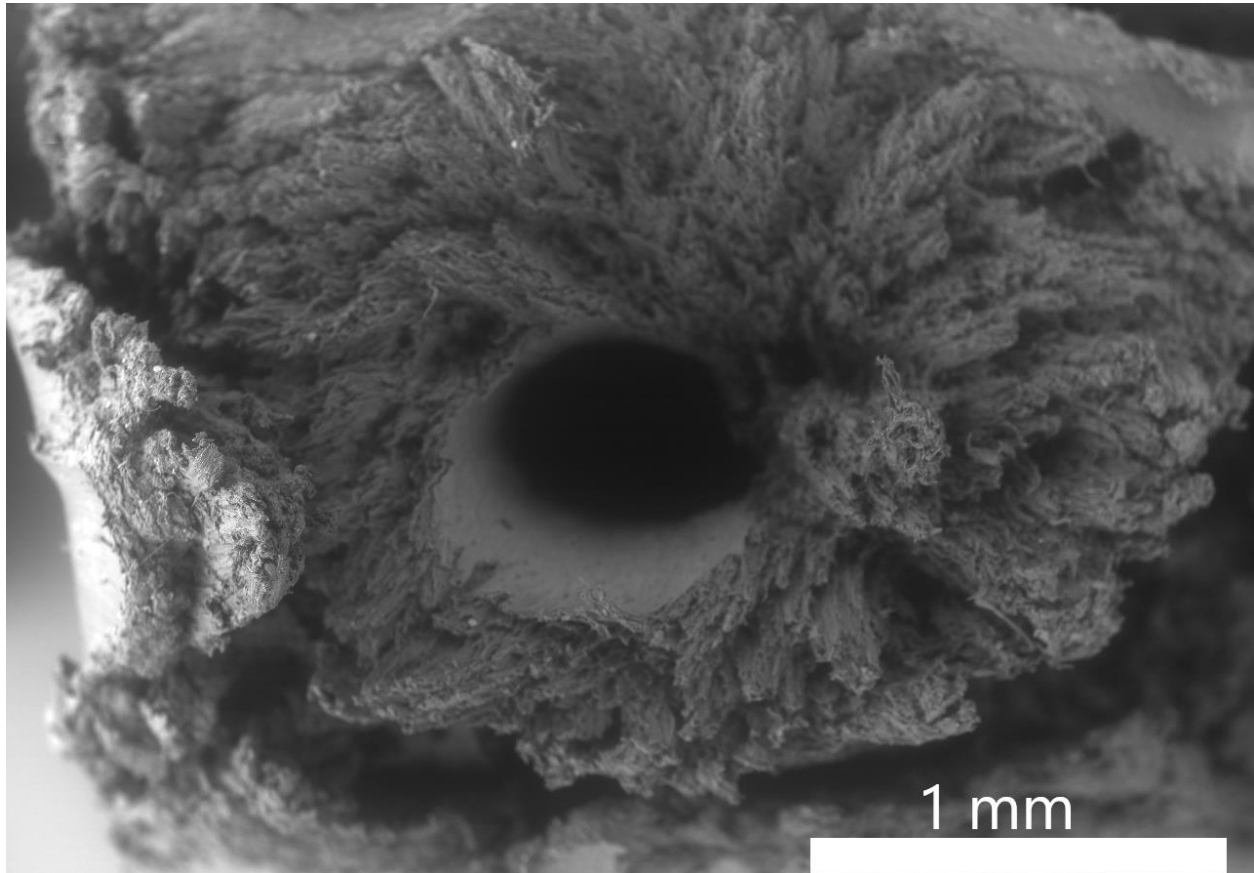
Figure 2.16 SEM image showing hollow core of gauge length in injection molded PLA/SEBS sample.

The ABS/SEBS blend showed very consistent fracture surfaces in both manufacturing methods with a predominance of ductile failure features. The as-printed sample shows slightly more deformation than the recovered sample which shows the interbead voids much more clearly.

The fracture evidence is as-expected for this polymer blend with mostly ductile evidence without extensive deformation. The injection molded samples show a fracture surface consisting of ductile fracture evidence and the presence of fibrils in the rupture areas as seen in Figure 2.15. The injection molded sample which was exposed to the shape memory testing exhibits some skin effect which presents itself as voids that run parallel to the mold walls and along the outer diameter of the sample gauge length as shown in Figure 2.16. This skin effect can be attributed the difference in cooling rate of the materials near the mold walls versus at the center.
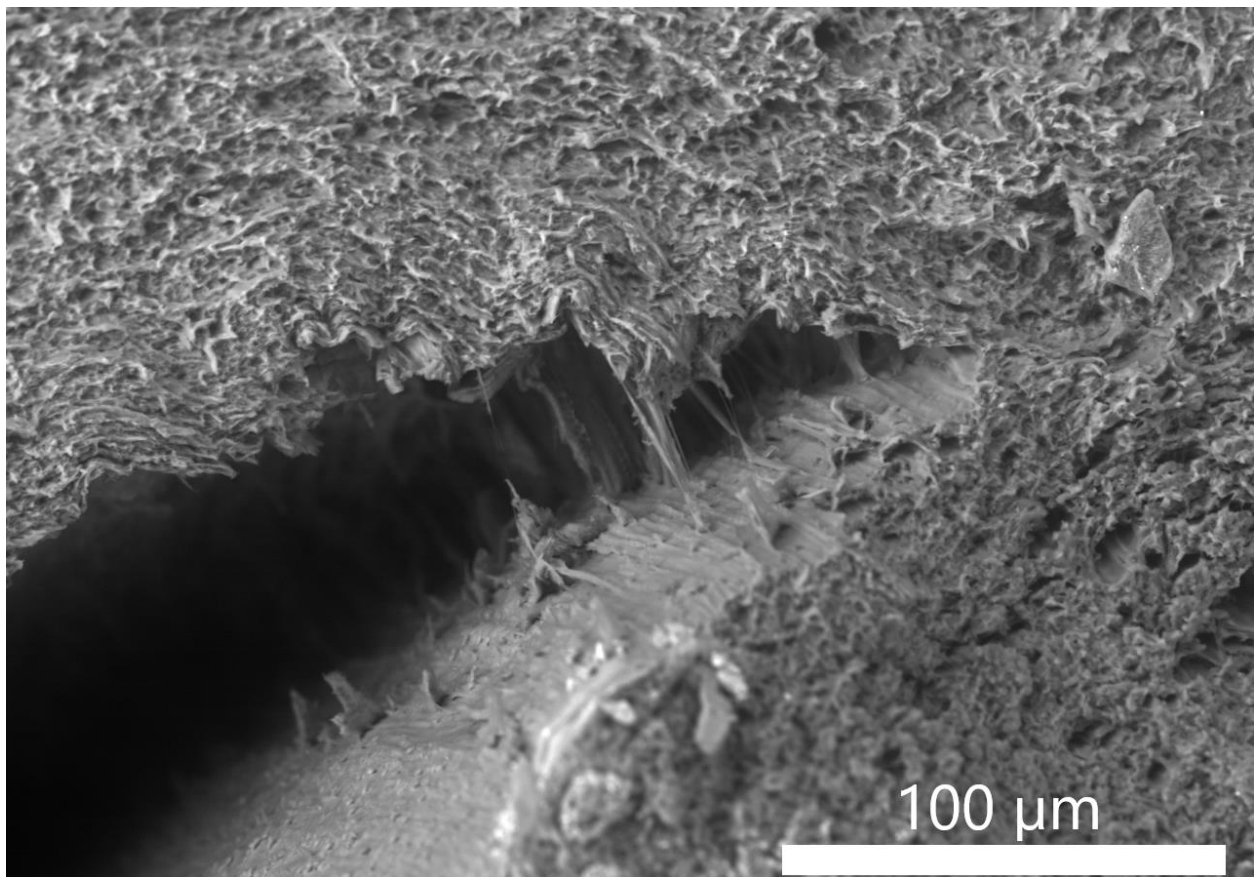
Figure 2.17 SEM image showing fibrils in the rupture area of an injection molded ABS/SEBS sample.
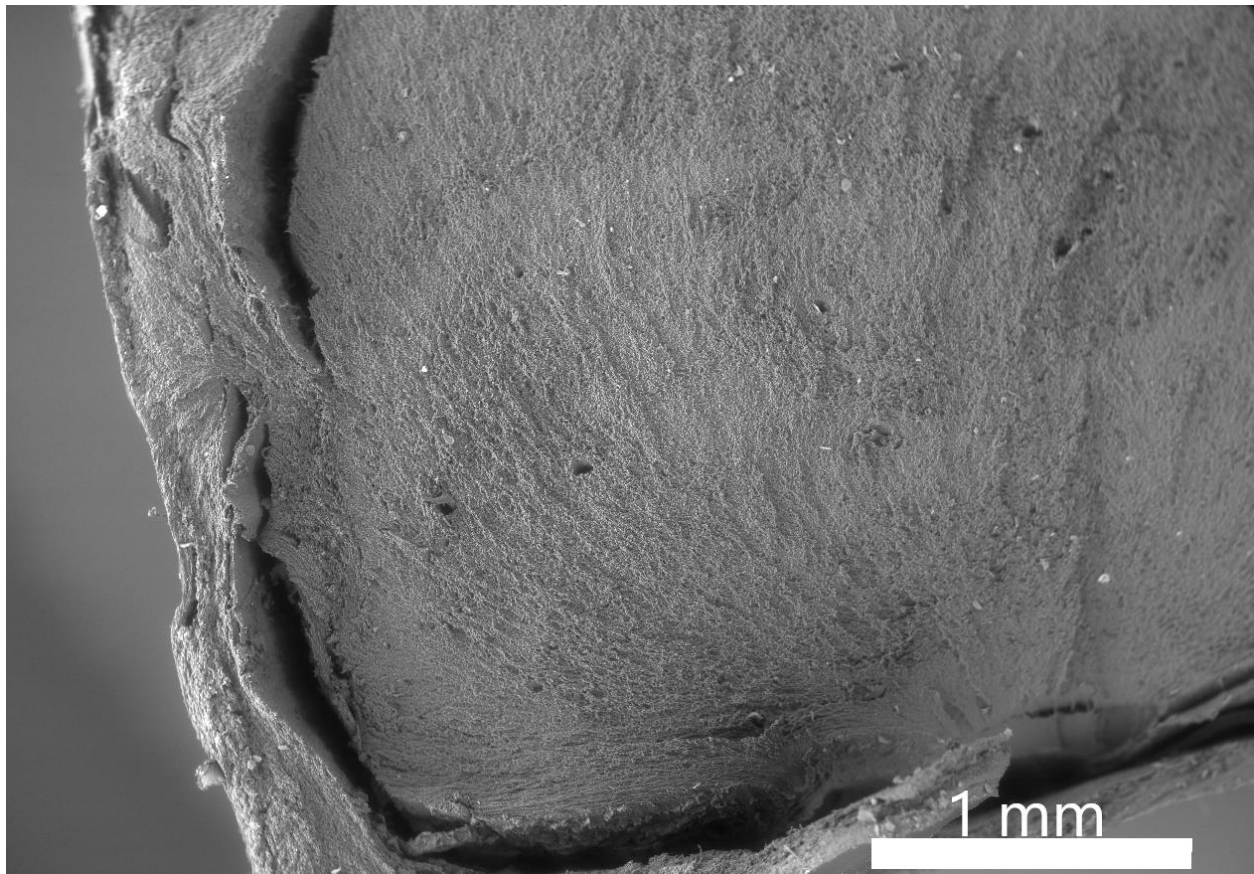
Figure 2.18 SEM image showing the voids along the outer diameter of the gauge length of an injection molded ABS/SEBS sample.

The last blend, PLA/TPU, shows very different fracture surface features between the 3D printed and the injection molded samples. The 3D printed samples show significant delamination between the layers of polymer and a great degree of deformation. These features are characteristic of a ductile fracture surface which is to be expected as this blend is 50% thermoplastic polyurethane by weight. There is very little difference in the fracture surface features between the samples that were tested as-printed and the samples that were subjected to the shape memory testing. The combination of the significant amount of plastic deformation and the presence of fibrils in the fracture surfaces indicate a ductile failure of the material. The batch of injection molded samples which was manufactured first and failed to test well due to lack of ductility shows

a very interesting fracture surface with evidence that may explain the poor test performance. The fracture surface shows almost 100% large fibrils that all appear disconnected from each other as seen in Figure 2.17. These features can be evidence for the possibility of the material absorbing moisture in the time between when it was dried before fabrication and when it was tested. PLA is hygroscopic and will absorb moisture from the air over time leading to a reduction in mechanical properties[54]. This batch of samples went the longest time between material drying and testing giving both hygroscopic materials in the blend plenty of time to absorb water and have their polymer chains broken leading to lower molecular weight and the performance exhibited in mechanical testing.
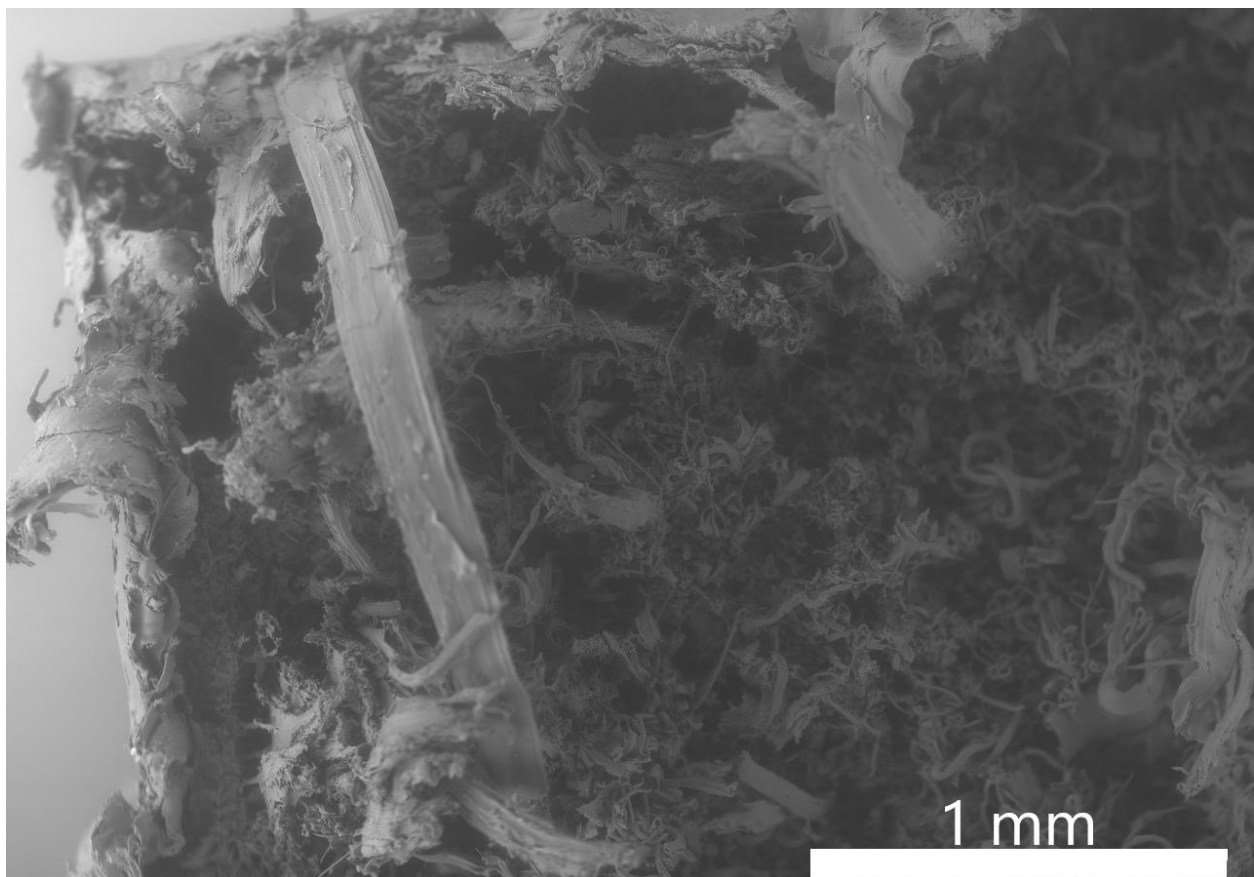
Figure 2.19 SEM image of the fracture surface from an injection molded PLA/TPU sample which failed to test well due to lack of ductility.

Conclusions

Mechanical properties of shape memory polymers are significantly affected by the amount of deformation from which they recover their shape. The results of this project attempts to create an objective metric by which we can evaluate the effect of shape memory recovery on the tensile strength of polymers. The results show that this effect varies depending on the materials used and their processing. The ABS/SEBS blend showed nearly no loss of strength in the 3D printed form after being recovered from varying amounts of deformation while the injection molded samples did show a decrease in average tensile strength. This shows a sensitivity to the manufacturing method of the samples for this polymer blend. The opposite is true of the PLA/SEBS blend in that it shows no sensitivity to manufacturing method but rather a sensitivity to whether or not the sample was allowed to dwell under load during deformation. The PLA/SEBS blend shows a worse healing parameter when dwell time is included in the test schedule and a better performance when there is no dwell time. However, dwell time had a significant effect on the shape memory properties of the blends, most noticeable by improving the fixation ratio across the board. The PLA/SEBS performed the best in shape memory characterization but not the best in healing parameter while the opposite is true of the ABS/SEBS blend which did not perform well as a shape memory polymer but performed very well in terms of healing parameter, particularly in the 3D printed form.

We can conclude from this study that good shape memory polymers don't necessarily make good self-healing parameter and vice-versa. Shape memory polymer research must continue in earnest so that we may quell the ever-increasing amount of polymer waste we generate as a civilization. I believe that evaluating materials by their healing parameter can be very useful in developing polymer systems which make products with significantly longer lifespans thanks to their ability to sef-heal.

References

1.   T. J. Word, A. Guerrero, & D. A. Roberson, Novel polymer materials systems to expand the capabilities of FDM^{TM}-type additive manufacturing. *MRS Communications*, **11** (2021) 129–145. https://doi.org/10.1557/s43579-021-00011-5.

2.   M. Kreiger & J. M. Pearce, Environmental impacts of distributed manufacturing from 3-D printing of polymer components and products. *Mater. Res. Soc. Symp. Proc.* (2013), pp. 85–90. https://doi.org/10.1557/opl.2013.319.

3.   R. Jones, P. Haufe, E. Sells, P. Iravani, V. Olliver, C. Palmer, & A. Bowyer, Reprap - The replicating rapid prototyper. *Robotica*, **29** (2011) 177–191. https://doi.org/10.1017/S026357471000069X.

4.   S. S. Crump, Modeling apparatus for three-dimensional objects. (1994).

5.   3D Printing Materials Guide: Plastics - 3Dnatives. (n.d.). https://www.3dnatives.com/en/plastics-used-3d-printing110420174/ (accessed September 18, 2020).

6.   S. H. Masood & W. Q. Song, Development of new metal/polymer materials for rapid tooling using Fused deposition modelling. *Materials & Design*, **25** (2004) 587–594. https://doi.org/10.1016/j.matdes.2004.02.009.

7.   W. q. Song & S. h. Masood, Thermal characteristics of a new metal/polymer material for FDM rapid prototyping process. *Assembly Automation*, **25** (2005) 309–315. https://doi.org/10.1108/01445150510626451.

8.   B. Khatri, K. Lappe, M. Habedank, T. Mueller, C. Megnin, & T. Hanemann, Fused Deposition Modeling of ABS-Barium Titanate Composites: A Simple Route towards Tailored Dielectric Devices. *Polymers*, **10** (2018) 666. https://doi.org/10.3390/polym10060666.

9.   H. Kim, J. Johnson, L. A. Chavez, C. A. Garcia Rosales, T. L. B. Tseng, & Y. Lin, Enhanced dielectric properties of three phase dielectric MWCNTs/BaTiO3/PVDF nanocomposites for energy storage using fused deposition modeling 3D printing. *Ceramics International*, **44** (2018) 9037–9044. https://doi.org/10.1016/j.ceramint.2018.02.107.

10.   V. Tambrallimath, R. Keshavamurthy, S. D, P. G. Koppad, & G. S. P. Kumar, Thermal behavior of PC-ABS based graphene filled polymer nanocomposite synthesized by FDM process. *Composites Communications*, **15** (2019) 129–134. https://doi.org/10.1016/j.coco.2019.07.009.

11.   H. L. Tekinalp, V. Kunc, G. M. Velez-Garcia, C. E. Duty, L. J. Love, A. K. Naskar, C. A. Blue, & S. Ozcan, Highly oriented carbon fiber-polymer composites via additive manufacturing. *Composites Science and Technology*, **105** (2014) 144–150. https://doi.org/10.1016/j.compscitech.2014.10.009.

12.   H. K. Sezer & O. Eren, FDM 3D printing of MWCNT re-inforced ABS nano-composite parts with enhanced mechanical and electrical properties. *Journal of Manufacturing Processes*, **37** (2019) 339–347. https://doi.org/10.1016/j.jmapro.2018.12.004.

13.   D20 Committee, *Test Method for Tensile Properties of Plastics*. https://doi.org/10.1520/D0638-14.

14.   D20 Committee, *Test Methods for Determining the Izod Pendulum Impact Resistance of Plastics*. https://doi.org/10.1520/D0256-10R18.

15.   The Science and Engineering of Materials, 7th Edition - 9781305076761 - Cengage. (n.d.). https://www.cengage.com/c/the-science-and-engineering-of-materials-7e-askeland/9781305076761/ (accessed September 22, 2020).

16.   W. Brostow, R. Chiu, I. M. Kalogeras, & A. Vassilikou-Dova, Prediction of glass transition temperatures: Binary blends and copolymers. *Materials Letters*, **62** (2008) 3152–3155. https://doi.org/10.1016/j.matlet.2008.02.008.

17.   David Roberson, Corey M Shemelya, Eric MacDonald, & Ryan Wicker, Expanding the applicability of FDM-type technologies through materials development. *Rapid Prototyping Journal*, **21** (2015) 137–143. https://doi.org/10.1108/RPJ-12-2014-0165.

18.   O. S. Es-Said, J. Foyos, R. Noorani, M. Mendelson, R. Marloth, & B. A. Pregger, Effect of Layer Orientation on Mechanical Properties of Rapid Prototyped Samples. *Materials and Manufacturing Processes*, **15** (2000) 107–122. https://doi.org/10.1080/10426910008912976.

19.   Anna Bellini & Selçuk Güçeri, Mechanical characterization of parts fabricated using fused deposition modeling. *Rapid Prototyping Journal*, **9** (2003) 252–264. https://doi.org/10.1108/13552540310489631.

20.   Sung-Hoon Ahn, Michael Montero, Dan Odell, Shad Roundy, & Paul K. Wright, Anisotropic material properties of fused deposition modeling ABS. *Rapid Prototyping Journal*, **8** (2002) 248–257. https://doi.org/10.1108/13552540210441166.

21.   V. Vega, J. Clements, T. Lam, A. Abad, B. Fritz, N. Ula, & O. S. Es-Said, The Effect of Layer Orientation on the Mechanical Properties and Microstructure of a Polymer. *J. of Materi Eng and Perform*, **20** (2011) 978–988. https://doi.org/10.1007/s11665-010-9740-z.

22.   R. Hague *, S. Mansour, & N. Saleh, Material and design considerations for rapid manufacturing. *International Journal of Production Research*, **42** (2004) 4691–4708. https://doi.org/10.1080/00207840410001733940.

23.   B. Caulfield, P. E. McHugh, & S. Lohfeld, Dependence of mechanical properties of polyamide components on build parameters in the SLS process. *Journal of Materials Processing Technology*, **182** (2007) 477–488. https://doi.org/10.1016/j.jmatprotec.2006.09.007.

24.   S. Shaffer, K. Yang, J. Vargas, M. A. Di Prima, & W. Voit, On reducing anisotropy in 3D printed polymers via ionizing radiation. *Polymer*, **55** (2014) 5969–5979. https://doi.org/10.1016/j.polymer.2014.07.054.

25.   A. Ravi, *A Study on an In-Process Laser Localized Pre-Deposition Heating Approach to Reducing FDM Part Anisotropy Water Film based Windows View project Exploration of Cost Reducion Techniques to speed up Solar adoption in the Residential Marketplace View project*.

26.   A. R. Torrado Perez, D. A. Roberson, & R. B. Wicker, Fracture surface analysis of 3D-printed tensile specimens of novel ABS-based materials. *Journal of Failure Analysis and Prevention*, **14** (2014) 343–353. https://doi.org/10.1007/s11668-014-9803-9.

27.   A. R. Torrado, C. M. Shemelya, J. D. English, Y. Lin, R. B. Wicker, & D. A. Roberson, Characterizing the effect of additives to ABS on the mechanical property anisotropy of specimens fabricated by material extrusion 3D printing. *Additive Manufacturing*, **6** (2015) 16–29. https://doi.org/10.1016/j.addma.2015.02.001.

28.   C. R. Rocha, A. R. T. Perez, D. A. Roberson, C. M. Shemelya, E. MacDonald, & R. B. Wicker, Novel ABS-based binary and ternary polymer blends for material extrusion 3D printing. *Journal of Materials Research*, **29** (2014) 1859–1866. https://doi.org/10.1557/jmr.2014.158.

29.   D. A. Quiñonez, Paulina A. Bermudez, Diego Ugarte-Sanchez, Leticia Roberson, Tailoring Physical Properties of Shape Memory Polymers for FDM-type Additive Manufacturing. *Solid Free. Fabr. 2019 Proc. 30th Annu. Inernational Solid Free. Fabr. Sumpos.* (Austin, TX USA: TMS, 2019), pp. 843–855.

30.   K. Elkins, H. Nordby2, C. Janak, R. W. Gray Iv, J. H. B0hn, & D. G. Baird, *Soft Elastomers for Fused Deposition Modeling*.

31.   V. Schimpf, J. B. Max, B. Stolz, B. Heck, & R. Mülhaupt, Semicrystalline Non-Isocyanate Polyhydroxyurethanes as Thermoplastics and Thermoplastic Elastomers and Their Use in 3D Printing by Fused Filament Fabrication. *Macromolecules*, **52** (2019) 320–331. https://doi.org/10.1021/acs.macromol.8b01908.

32.   A. Hary´nska, H. Hary´nska, J. Kucinska-Lipka, A. Sulowska, I. Gubanska, M. Kostrzewa, & H. Janik, materials Medical-Grade PCL Based Polyurethane System for FDM 3D Printing-Characterization and Fabrication. (2019). https://doi.org/10.3390/ma12060887.

33.   J. G. Siqueiros, K. Schnittker, & D. A. Roberson, ABS-maleated SEBS blend as a 3D printable material. *Virtual and Physical Prototyping*, **11** (2016) 123–131.

34.   T. Reppel & K. Weinberg, Experimental determination of elastic and rupture properties of printed Ninjaflex. *Technische Mechanik*, **38** (2018) 104–112. https://doi.org/10.24352/UB.OVGU-2018-010.

35.   D. A. Roberson & J. G. Siqueiros, Novel Polycarbonate/SEBS-g-MA Blend for FDM-Type 3D Printing. (ANTEC, 2016).

36.   Y. Yang, Y. Chen, Y. Wei, & Y. Li, 3D printing of shape memory polymer for functional part fabrication. *Int J Adv Manuf Technol*, **84** (2016) 2079–2095. https://doi.org/10.1007/s00170-015-7843-2.

37.   J. Raasch, M. Ivey, D. Aldrich, D. S. Nobes, & C. Ayranci, Characterization of polyurethane shape memory polymer processed by material extrusion additive manufacturing. *Additive Manufacturing*, **8** (2015) 132–141. https://doi.org/10.1016/j.addma.2015.09.004.

38.   F. A. Chávez, J. G. Siqueiros, I. A. Carrete, I. L. Delgado, G. W. Ritter, & D. A. Roberson, Characterisation of phases and deformation temperature for additively manufactured shape memory polymer components fabricated from rubberised acrylonitrile butadiene styrene. *Virtual and Physical Prototyping*, **14** (2019) 188–202. https://doi.org/10.1080/17452759.2018.1550694.

39.   A. R. Torrado & D. A. Roberson, Failure Analysis and Anisotropy Evaluation of 3D-Printed Tensile Test Specimens of Different Geometries and Print Raster Patterns. *J Fail. Anal. and Preven.*, **16** (2016) 154–164. https://doi.org/10.1007/s11668-016-0067-4.

40. W. G. Yang, H. Lu, W. M. Huang, H. J. Qi, X. L. Wu, & K. Y. Sun, Advanced Shape Memory Technology to Reshape Product Design, Manufacturing and Recycling. *Polymers*, **6** (2014) 2287–2308. https://doi.org/10.3390/polym6082287.

41. P. Quinonez, Tailoring Physical Properties Of Shape Memory Polymers For FDM-Type Additive Manufacturing. *Open Access Theses & Dissertations*, (2019).

42. D. P. Schmitz, L. G. Ecco, S. Dul, E. C. L. Pereira, B. G. Soares, G. M. O. Barra, & A. Pegoretti, Electromagnetic interference shielding effectiveness of ABS carbon-based composites manufactured via fused deposition modelling. *Materials Today Communications*, **15** (2018) 70–80. https://doi.org/10.1016/j.mtcomm.2018.02.034.

43. C. M. Shemelya, A. Rivera, A. T. Perez, C. Rocha, M. Liang, X. Yu, C. Kief, D. Alexander, J. Stegeman, H. Xin, R. B. Wicker, E. MacDonald, & D. A. Roberson, Mechanical, Electromagnetic, and X-ray Shielding Characterization of a 3D Printable Tungsten–Polycarbonate Polymer Matrix Composite for Space-Based Applications. *Journal of Elec Materi*, **44** (2015) 2598–2607. https://doi.org/10.1007/s11664-015-3687-7.

44. Cullity, B.D. (1978) Elements of X-Ray Diffraction. 2nd Edition, Addison-Wesley Publishing Company Inc., Phillippines. - References - Scientific Research Publishing. (n.d.). https://www.scirp.org/(S(vtj3fa45qm1ean45vvffcz55))/reference/ReferencesPapers.aspx?ReferenceID=1301967 (accessed September 22, 2020).

45. J. Pakkanen, D. Manfredi, P. Minetola, & L. Iuliano, About the use of recycled or biodegradable filaments for sustainability of 3D printing: State of the art and research opportunities. *Smart Innov. Syst. Technol.* (Springer Science and Business Media Deutschland GmbH, 2017), pp. 776–785. https://doi.org/10.1007/978-3-319-57078-5_73.

46. J. Beniak, P. Križan, M. Matúš, & M. Šajgalík, Experimental testing of PLA biodegradable thermoplastic in the frame of 3D printing FDM technology. *MATEC Web of Conferences*, **157** (2018) 06001. https://doi.org/10.1051/matecconf/201815706001.

47. J. Korpela, A. Kokkari, H. Korhonen, M. Malin, T. Narhi, & J. Seppalea, Biodegradable and bioactive porous scaffold structures prepared using fused deposition modeling. *Journal of Biomedical Materials Research - Part B Applied Biomaterials*, **101** (2013) 610–619. https://doi.org/10.1002/jbm.b.32863.

48. N. E. Zander, M. Gillan, & R. H. Lambeth, Recycled polyethylene terephthalate as a new FFF feedstock material. *Additive Manufacturing*, **21** (2018) 174–182. https://doi.org/10.1016/j.addma.2018.03.007.

49. N. E. Zander, M. Gillan, Z. Burckhard, & F. Gardea, Recycled polypropylene blends as novel 3D printing materials. *Additive Manufacturing*, **25** (2019) 122–130. https://doi.org/10.1016/j.addma.2018.11.009.

50. K.-L. G. Ho, A. L. Pometto, A. Gadea-Rivas, J. A. Briceño, & A. Rojas, Degradation of Polylactic Acid (PLA) Plastic in Costa Rican Soil and Iowa State University Compost Rows. *Journal of Polymers and the Environment*, **7** (1999) 173–177. https://doi.org/10.1023/A:1022874530586.

51.   C. R. Rocha Gutierrez, Improving the engineering properties of PLA for 3D printing and beyond, The University of Texas at El Paso, 2016.

52.   I. A. Carrete, P. A. Quiñonez, D. Bermudez, & D. A. Roberson, Incorporating Textile-Derived Cellulose Fibers for the Strengthening of Recycled Polyethylene Terephthalate for 3D Printing Feedstock Materials. *Journal of Polymers and the Environment*, (2020) 1–10. https://doi.org/10.1007/s10924-020-01900-x.

53.   Israel A. Carrete, Development and Characterization of Polyethylene Terephalate (PET)-Cotton Natural Fiber-Reinforced Composites from Waste Materials, The University of Texas at El Paso, 2019.

54.   J. G. Siqueiros & D. A. Roberson, In Situ Wire Drawing of Phosphate Glass in Polymer Matrices for Material Extrusion 3D Printing. *International Journal of Polymer Science*, **2017** (2017).

55.   Biaxially oriented poly(propylene-g-maleic anhydride)/phosphate glass composite films for high gas barrier applications | Elsevier Enhanced Reader. (n.d.). https://reader.elsevier.com/reader/sd/pii/S0032386108010197?token=BBC87C8306E79ADC1F4A1C43B 72C1233A4C3E53BC17C43850D22C982E8B01E7CD76559BE631ECC66235FC1D064F9A97C (accessed September 23, 2020).

56.   F. A. Chávez, P. A. Quiñonez, & D. A. Roberson, Hybrid metal/thermoplastic composites for FDM-type additive manufacturing. *Journal of Thermoplastic Composite Materials*, (2019) 089270571986415. https://doi.org/10.1177/0892705719864150.

57.   I. A. Carrete, D. Bermudez, C. Aguirre, F. A. Alvarez-Primo, S. Anil-Kumar, P. Chinolla, M. Gamboa, S. A. Gonzalez, H. E. Heredia, A. M. Hernandez, E. Levario, J. R. Lindquist, V. C. Luna, L. M. Martinez, V. E. Mendez, J. J. Slager, L. Ugarte-Sanchez, Y. A. Urquidi, A. Zamora, & D. A. Roberson, Failure Analysis of Additively Manufactured Polyester Test Specimens Exposed to Various Liquid Media. *J Fail. Anal. and Preven.*, (2019). https://doi.org/10.1007/s11668-019-00614-0.

58.   D. Hosler, S. L. Burkett, & M. J. Tarkanian, Prehistoric Polymers: Rubber Processing in Ancient Mesoamerica. *Science*, **284** (1999) 1988–1991. https://doi.org/10.1126/science.284.5422.1988.

59.   Andrady Anthony L. & Neal Mike A., Applications and societal benefits of plastics. *Philosophical Transactions of the Royal Society B: Biological Sciences*, **364** (2009) 1977–1984. https://doi.org/10.1098/rstb.2008.0304.

60.   I. Carrete, Development and Characterization of Polyethylene Terephthalate (PET)-Cotton Natural Fiber-Reinforced Composites From Waste Materials. *Open Access Theses & Dissertations*, (2019).

61.   I. A. Carrete, P. A. Quiñonez, D. Bermudez, & D. A. Roberson, Incorporating Textile-Derived Cellulose Fibers for the Strengthening of Recycled Polyethylene Terephthalate for 3D Printing Feedstock Materials. *Journal of Polymers and the Environment*, **29** (2021) 662–671. https://doi.org/10.1007/s10924-020-01900-x.

62.   J. R. Jambeck, R. Geyer, C. Wilcox, T. R. Siegler, M. Perryman, A. Andrady, R. Narayan, & K. L. Law, Plastic waste inputs from land into the ocean. *Science*, **347** (2015) 768–771. https://doi.org/10.1126/science.1260352.

63.   E. Fries, J. H. Dekiff, J. Willmeyer, M.-T. Nuelle, M. Ebert, & D. Remy, Identification of polymer types and additives in marine microplastic particles using pyrolysis-GC/MS and scanning electron microscopy. *Environmental Science: Processes & Impacts*, **15** (2013) 1949–1956. https://doi.org/10.1039/C3EM00214D.

64.   P. Schwabl, S. Köppel, P. Königshofer, T. Bucsics, M. Trauner, T. Reiberger, & B. Liebmann, Detection of Various Microplastics in Human Stool. *Annals of Internal Medicine*, **171** (2019) 453–457. https://doi.org/10.7326/M19-0618.

65.   F. Pérez-Guevara, G. Kutralam-Muniasamy, & V. C. Shruti, Critical review on microplastics in fecal matter: Research progress, analytical methods and future outlook. *Science of The Total Environment*, **778** (2021) 146395. https://doi.org/10.1016/j.scitotenv.2021.146395.

66.   Z. Yan, Y. Liu, T. Zhang, F. Zhang, H. Ren, & Y. Zhang, Analysis of Microplastics in Human Feces Reveals a Correlation between Fecal Microplastics and Inflammatory Bowel Disease Status. *Environmental Science & Technology*, **56** (2022) 414–421. https://doi.org/10.1021/acs.est.1c03924.

67.   N. Zhang, Y. B. Li, H. R. He, J. F. Zhang, & G. S. Ma, You are what you eat: Microplastics in the feces of young men living in Beijing. *Science of The Total Environment*, **767** (2021) 144345. https://doi.org/10.1016/j.scitotenv.2020.144345.

68.   A. Ragusa, A. Svelato, C. Santacroce, P. Catalano, V. Notarstefano, O. Carnevali, F. Papa, M. C. A. Rongioletti, F. Baiocco, S. Draghi, E. D'Amore, D. Rinaldo, M. Matta, & E. Giorgini, Plasticenta: First evidence of microplastics in human placenta. *Environment International*, **146** (2021) 106274. https://doi.org/10.1016/j.envint.2020.106274.

69.   H. A. Leslie, M. J. M. van Velzen, S. H. Brandsma, D. Vethaak, J. J. Garcia-Vallejo, & M. H. Lamoree, Discovery and quantification of plastic particle pollution in human blood. *Environment International*, (2022) 107199. https://doi.org/10.1016/j.envint.2022.107199.

70.   L. C. Jenner, J. M. Rotchell, R. T. Bennett, M. Cowen, V. Tentzeris, & L. R. Sadofsky, Detection of microplastics in human lung tissue using µFTIR spectroscopy. *Science of The Total Environment*, **831** (2022) 154907. https://doi.org/10.1016/j.scitotenv.2022.154907.

71.   K. J. McDermid & T. L. McMullen, Quantitative analysis of small-plastic debris on beaches in the Hawaiian archipelago. *Marine Pollution Bulletin*, **48** (2004) 790–794. https://doi.org/10.1016/j.marpolbul.2003.10.017.

72.   J. G. B. Derraik, The pollution of the marine environment by plastic debris: a review. *Marine Pollution Bulletin*, **44** (2002) 842–852. https://doi.org/10.1016/S0025-326X(02)00220-5.

73.   P. G. Ryan, C. J. Moore, J. A. van Franeker, & C. L. Moloney, Monitoring the abundance of plastic debris in the marine environment. *Philosophical Transactions of the Royal Society of London B: Biological Sciences*, **364** (2009) 1999–2012. https://doi.org/10.1098/rstb.2008.0207.

74.   H. Hirai, H. Takada, Y. Ogata, R. Yamashita, K. Mizukawa, M. Saha, C. Kwan, C. Moore, H. Gray, D. Laursen, E. R. Zettler, J. W. Farrington, C. M. Reddy, E. E. Peacock, & M. W. Ward, Organic micropollutants in marine plastics debris from the open ocean and remote and urban beaches. *Marine Pollution Bulletin*, **62** (2011) 1683–1692. https://doi.org/10.1016/j.marpolbul.2011.06.004.

75.   J. Kaiser, The Dirt on Ocean Garbage Patches. *Science*, **328** (2010) 1506–1506. https://doi.org/10.1126/science.328.5985.1506.

76.   S. Morét-Ferguson, K. L. Law, G. Proskurowski, E. K. Murphy, E. E. Peacock, & C. M. Reddy, The size, mass, and composition of plastic debris in the western North Atlantic Ocean. *Marine Pollution Bulletin*, **60** (2010) 1873–1878. https://doi.org/10.1016/j.marpolbul.2010.07.020.

77.   S. L. Dautel, Transoceanic Trash: International and United States Strategies for the Great Pacific Garbage Patch Farming and Food: How We Grow What We Eat: Comment. *Golden Gate University Environmental Law Journal*, **3** (2009) 181–208.

78.   J. Zalasiewicz, C. N. Waters, J. A. Ivar do Sul, P. L. Corcoran, A. D. Barnosky, A. Cearreta, M. Edgeworth, A. Gałuszka, C. Jeandel, R. Leinfelder, J. R. McNeill, W. Steffen, C. Summerhayes, M. Wagreich, M. Williams, A. P. Wolfe, & Y. Yonan, The geological cycle of plastics and their use as a stratigraphic indicator of the Anthropocene. *Anthropocene*, **13** (2016) 4–17. https://doi.org/10.1016/j.ancene.2016.01.002.

79.   L. Shen & E. Worrell, Chapter 13 - Plastic Recycling. In E. Worrell, & M.A. Reuter,eds., *Handb. Recycl.* (Boston: Elsevier, 2014), pp. 179–190. https://doi.org/10.1016/B978-0-12-396459-5.00013-1.

80.   C. Jehanno, J. W. Alty, M. Roosen, S. De Meester, A. P. Dove, E. Y.-X. Chen, F. A. Leibfarth, & H. Sardon, Critical advances and future opportunities in upcycling commodity polymers. *Nature*, **603** (2022) 803–814. https://doi.org/10.1038/s41586-021-04350-0.

81.   X. L. Wu, W. M. Huang, & H. X. Tan, Characterization of shape recovery via creeping and shape memory effect in ether-vinyl acetate copolymer (EVA). *Journal of Polymer Research*, **20** (2013) 150. https://doi.org/10.1007/s10965-013-0150-4.

82.   P. A. Quiñonez, L. Ugarte-Sanchez, D. Bermudez, P. Chinolla, R. Dueck, T. J. Cavender-Word, & D. A. Roberson, Design of Shape Memory Thermoplastic Material Systems for FDM-Type Additive Manufacturing. *Materials*, **14** (2021) 4254. https://doi.org/10.3390/ma14154254.

83.   F. A. Chávez, J. G. Siqueiros, I. A. Carrete, I. L. Delgado, G. W. Ritter, & D. A. Roberson, Characterisation of phases and deformation temperature for additively manufactured shape memory polymer components fabricated from rubberised acrylonitrile butadiene styrene. *Virtual and Physical Prototyping*, **0** (2018) 1–15. https://doi.org/10.1080/17452759.2018.1550694.

84.   Jorge Mario Avila Barraza, Exploring the Effect of Environmental Degradation on the Shape Memory Properties of Polymers, The University of Texas at El Paso, 2022.

85.   W. G. Yang, H. Lu, W. M. Huang, H. J. Qi, X. L. Wu, & K. Y. Sun, Advanced Shape Memory Technology to Reshape Product Design, Manufacturing and Recycling. *Polymers*, **6** (2014) 2287–2308. https://doi.org/10.3390/polym6082287.

86.   S.-M. Lai & Y.-C. Lan, Shape memory properties of melt-blended polylactic acid (PLA)/thermoplastic polyurethane (TPU) bio-based blends. *Journal of Polymer Research*, **20** (2013) 140. https://doi.org/10.1007/s10965-013-0140-6.

87.   T. Xie, Recent advances in polymer shape memory. *Polymer*, **52** (2011) 4985–5000. https://doi.org/10.1016/j.polymer.2011.08.003.

88.   B. K. Kim, S. Y. Lee, & M. Xu, Polyurethanes having shape memory effects. *Polymer*, **37** (1996) 5781–5793. https://doi.org/10.1016/S0032-3861(96)00442-9.

89.   A. Lendlein & S. Kelch, Shape-Memory Polymers. *Angewandte Chemie*, **41** (2002) 2034–2057.

90.   D. L. Taylor & M. in het Panhuis, Self-Healing Hydrogels. *Advanced Materials*, **28** (2016) 9060–9093. https://doi.org/10.1002/adma.201601613.

91.   X. Xu, P. Fan, J. Ren, Y. Cheng, J. Ren, J. Zhao, & R. Song, Self-healing thermoplastic polyurethane (TPU)/polycaprolactone (PCL) /multi-wall carbon nanotubes (MWCNTs) blend as shape-memory composites. *Composites Science and Technology*, **168** (2018) 255–262. https://doi.org/10.1016/j.compscitech.2018.10.003.

92.   R. P. Wool & K. M. O'Connor, A theory crack healing in polymers. *Journal of Applied Physics*, **52** (1981) 5953–5963. https://doi.org/10.1063/1.328526.

93.   X. Jian, Y. Hu, W. Zhou, & L. Xiao, Self-healing polyurethane based on disulfide bond and hydrogen bond. *Polymers for Advanced Technologies*, **29** (2018) 463–469. https://doi.org/10.1002/pat.4135.

94.   J. G. Siqueiros, K. Schnittker, & D. A. Roberson, ABS-maleated SEBS blend as a 3D printable material. *Virtual and Physical Prototyping*, **11** (2016) 123–131. https://doi.org/10.1080/17452759.2016.1175045.

95.   D. Roberson & J. Siqueiros, Novel Polycarbonate/SEBS-g-MA Blend for FDM-Type 3D Printing. (Indianapolis, IN: SPE, 2016).

96.   C. R. Rocha, A. R. T. Perez, D. A. Roberson, C. M. Shemelya, E. MacDonald, & R. B. Wicker, Novel ABS-based binary and ternary polymer blends for material extrusion 3D printing. *Journal of Materials Research*, **29** (2014) 1859–1866. https://doi.org/10.1557/jmr.2014.158.

97.   A. R. Torrado, C. M. Shemelya, J. D. English, Y. Lin, R. B. Wicker, & D. A. Roberson, Characterizing the effect of additives to ABS on the mechanical property anisotropy of specimens fabricated by material extrusion 3D printing. *Additive Manufacturing*, **6** (2015) 16–29. https://doi.org/10.1016/j.addma.2015.02.001.

98.   D. A. Roberson, K. Schnittker, & J. G. Siqueiros, Methods and polymer compositions for material extrusion 3D printing. (2021).

99.   D20 Committee, *Test Method for Tensile Properties of Plastics* (ASTM International). https://doi.org/10.1520/D0638-14.

100.   D30 Committee, *Test Method for Glass Transition Temperature (DMA Tg) of Polymer Matrix Composites by Dynamic Mechanical Analysis (DMA)* (ASTM International). https://doi.org/10.1520/D7028-07E01.

101.   A. R. Torrado & D. A. Roberson, Failure Analysis and Anisotropy Evaluation of 3D-Printed Tensile Test Specimens of Different Geometries and Print Raster Patterns. *Journal of Failure Analysis and Prevention*, **16** (2016) 154–164. https://doi.org/10.1007/s11668-016-0067-4.

102.   J. M. Avila, T. J. Cavender-Word, & D. A. Roberson, Exploring the Effect of Moisture Exposure on Shape Memory Polymer Performance. *Journal of Polymers and the Environment*, (2023). https://doi.org/10.1007/s10924-023-02818-w.

103.   C. R. Rocha Gutierrez, Improving the engineering properties of PLA for 3D printing and beyond, Ph.D., The University of Texas at El Paso, 2016.

104.   D. Bermudez, P. A. Quiñonez, E. J. Vasquez, I. A. Carrete, T. J. Word, & D. A. Roberson, A Comparison of the physical properties of two commercial 3D printing PLA grades. *Virtual and Physical Prototyping*, **16** (2021) 178–195. https://doi.org/10.1080/17452759.2021.1910047.

105.   Standard Practice for Plastics: Dynamic Mechanical Properties: Determination and Report of Procedures. (n.d.). https://www.astm.org/d4065-20.html (accessed May 3, 2023).

Appendix

License for use of published article for Chapter 1 of this dissertation.

Vita

Truman James Word was born on February 24th, 1993 in El Paso, TX. He is the only child to parents Glen and Diane Word. He graduated from Coronado High School in June 2010 before attending Austin College in Sherman, TX to continue his swimming career and earn his bachelor's degree. He graduated from Austin College in May 2014 with a Bachelor's degree majoring in Economics and minoring Chemistry while serving as the men's swim team captain his senior year. He took a gap year in which he worked while applying for law school. He was accepted to Baylor and Pepperdine before deciding against law school. He began his second bachelor's degree at the University of Texas at El Paso in August 2015 where he pursued a degree in Metallurgical and Materials Engineering. He had two internships, one with NASA and one with Nucor Steel, before graduating Magna Cum Laude with his second bachelor's degree in May 2018.

Truman's passions consist of swimming, aviation, photography/videography, and lifting weights amongst other things. He has been coaching competitive swimming in El Paso since August 2017 for the Barracuda Aquatics Team of which he is a former member. Under the mentorship of Coach Wright Stanton III, he has had the opportunity to coach from the learn-to-swim level all the way up to the national level. He has also competed at the national level multiple times in the United States Masters Swimming Spring National Championship. He earned his private pilots license in July 2010 with a fixed wing rating then added on his private lighter than air (LTA) rating in June 2020 to fly hot air balloons. Truman and his father fly in the Albuquerque International Balloon Fiesta every year in October.

word.truman@gmail.com